Small-animal SPECT with Two Stationary Detectors: Performance

Evaluation and Image Quality Assessment of Multi-pinhole Collimators

-

Kleintier-SPECT mit Zwei Stationären Detektoren: Leistungsbewertung

und Bildqualitätsanalyse von Multipinhole-Kollimatoren

Doctoral thesis for a medical doctoral degree

at the Graduate School of Life Sciences,

Julius-Maximilians-Universität Würzburg,

Section Clinical Sciences

submitted by

Jan Vincent Hoffmann

from

Nuremberg

Würzburg **2023**

Submitted on:

…………………………………………………..……..
     Office stamp

Members of the Thesis Committee:

Chairperson: Prof. Dr. rer. nat. C. Otto

Primary Supervisor: Professor Dr. med. A. Buck

Supervisor (Second): Prof. T. Higuchi, MD, PhD

Supervisor (Third): Prof. Dr. rer. nat. H. Köstler

Date of Public Defence: …………………………………….…………

Date of Receipt of Certificates:

………………………………………….

Affidavit

I hereby confirm that my thesis *"Small-animal SPECT with Two Stationary Detectors: Performance Evaluation and Image Quality Assessment of Multi-pinhole Collimators"* is the result of my own work. I did not receive any help or support from commercial consultants. All sources and/or materials applied are listed and specified in the thesis.

Furthermore, I confirm that this thesis has not yet been submitted as part of another examination process neither in identical nor in similar form.

Place, Date   Signature

Eidesstattliche Erklärung

Hiermit erkläre ich an Eides statt, die Dissertation *„Kleintier-SPECT mit Zwei Stationären Detektoren: Leistungsbewertung und Bildqualitätsanalyse von Multipinhole-Kollimatoren"* eigenständig, d.h. insbesondere selbständig und ohne Hilfe eines kommerziellen Promotionsberaters, angefertigt und keine anderen als die von mir angegebenen Quellen und Hilfsmittel verwendet zu haben.

Ich erkläre außerdem, dass die Dissertation weder in gleicher noch in ähnlicher Form bereits in einem anderen Prüfungsverfahren vorgelegen hat.

Ort, Datum   Unterschrift

Dedication

I would like to dedicate my work to my parents, as they have always stood and continue to stand by my side with unconditional support. They were the ones who made it possible for me to do this work in the first place, but even more importantly, they supported me throughout my medical studies.

I am proud to have such parents.
All that I have achieved so far in my life would not have been conceivable without you in any way.

Thank you from my heart.

Table of Contents

1. Introduction

In recent years, nuclear medicine with its molecular imaging technologies single photon emission computed tomography (SPECT), and positron emission tomography (PET) recorded significantly increasing interest both in clinical practice and in preclinical research [1]. The major advantage of emission tomography is that it can image functional processes in organisms even at the subcellular level, since the applied radiotracers are involved in the metabolism of the organism of interest, be it human or small animal.

If one compares the two main representatives, SPECT and PET, there are certain advantages on both sides. PET is often referred to as the gold standard in molecular imaging, as it is superior to its counterpart SPECT in both sensitivity and spatial resolution [2]. Although this may still be true in the clinical setting, this has changed dramatically in recent years with numerous advances in small-animal SPECT for preclinical research. Even though sensitivity was improved, it must be admitted that SPECT is still not able to keep up with PET [3], and the increase of spatial resolution is at the expense of sensitivity [4]. However, small fields of view (FOV) combined with multi-pinhole collimation and large stationary detectors allow high magnification apertures and hence, SPECT is capable of submillimeter spatial resolution up to 0.25 mm in small rodents [5], whereas the resolution of collimated PET goes up to 0.75 mm in vivo [6], and in simulation studies, even resolutions of 0.5 mm have been achieved [7]. Moreover, single photon emission imaging allows the application of multiple radioisotopes at the same time, as each is characterized by unique photon energy. The possibility of dual-isotope imaging has been already demonstrated in animals [6, 8, 9], as in humans [10, 11].

In clinical practice, single photon emission imaging is an essential tool for non-invasive myocardial perfusion studies, diagnosis of somatostatin-receptor positive neuroendocrine tumors and adrenal tumors or paragangliomas, and staging of differentiated thyroid cancer, to name a few [12]. With the advances especially concerning spatial resolution in dedicated small-animal scanners, SPECT has also evolved into a powerful tool in preclinical research. As the administration of radiopharmaceuticals is carried out in vivo, this allows especially in the preclinical field to perform longitudinal studies more easily, and thus, molecular imaging is a good substitute for complex and labor-intensive ex vivo biodistribution studies [13].

Accordingly, the preclinical demand is constantly rising as molecular imaging enables non-invasive pharmacodynamic studies in the field of drug development [14, 15]. Furthermore, with this advancement, barriers to translational research have been reduced, giving a new boost to tracer development which will probably lead to an extended field of clinical application [16]. Moreover, the improved integration of computed tomography (CT) or magnetic resonance imaging (MRI) modules enables precise anatomical correlation and additionally allows the compensation of interferences like attenuation by the tissue [17-20]. Even though hybrid imaging with SPECT/CT is still not as established as PET/CT, recently published data shows that clinical usability of the obtained images significantly benefits from an anatomical co-registration using CT or even MRI [21-27]. Hence, an increase in the application of SPECT/CT in the clinical routine can be expected in the next years.

As reviewed by Van den Wyngaert et al. [28], Israel et al. [29], and Mariani et al. [30], published data shows potential for various clinical examinations using SPECT/CT hybrid imaging in the fields of oncology, cardiology, and neurology, to name a few.

With the advances in the collimator and detector design in combination with enhanced iterative reconstruction algorithms, small-animal SPECT is now capable of high spatial resolution with reasonable sensitivity without exposing animals to unnecessarily high radiation doses [16]. Recently, to ensure easy access to preclinical SPECT, manufacturers offer entry-level models, like the investigated system with two instead of three stationary detectors resulting in lower acquisition costs. Accordingly, the aim of this thesis is to prove whether these systems can still maintain their place in preclinical research.

Remark

The used methodology and parts of the results of this dissertation have been recently published by the European Association of Nuclear Medicine [31].

1.1. Basics of Imaging in Nuclear Medicine

Medical imaging can be divided into two main groups: conventional transmission and emission tomography. With CT scans, transmission imaging is the main feature in radiology, which is characterized by the fact that anatomical data can be visualized and diagnosed accordingly. This is based on the principle that both origin and detection location are known and an object, e.g., a patient, must be penetrated at different angles along the photons' trajectories so that the reconstructed images represent the distribution of attenuation coefficients. Imaging in nuclear medicine is based on the detection of emitted photons, either by gamma emission in SPECT or by positron emission in PET. In this process, the corresponding photons are detected without knowing their origin and directional information, which is why an estimate of the origin and thus an image of the radioactivity accumulation in the examined object must be reconstructed utilizing several imaging angles.

The general idea of emission tomography is based on the so-called tracer principle introduced by O. Chiewitz and G. Hevesy in 1935 [32]. This principle states that every radioisotope behaves chemically in the same way as the non-radioactive isotopes of the same element. Consequently, a radioisotope, e.g., 99m-technetium (^{99m}Tc), connected to a radiopharmaceutical can be applied, usually intravenously. After injection, the tracer will participate in the patient's metabolism. Like this, it will be distributed in the body and with a certain imaging device, emitted photons can be detected, and images can be created. This allows for the detection and visualization of certain functional processes in the patient's body. Due to the high detection efficiency of these emitted high-energetic photons, the applied amount of radiotracer can be kept very low. Hence, patients are exposed to a relatively modest radiation dose [33]. Further, theoretically, there is an infinite variety of tracers for imaging different biochemical processes as radioisotopes can be labeled to changing radiopharmaceuticals. In nuclear medicine photon emission tomography is used in two kinds of ways: SPECT and PET.

SPECT imaging makes use of radioisotopes which decay by emitting photons isotropically. Emitted photons each have an energy that is specific for the corresponding radioisotope. This enables a unique possibility compared to its rival PET as multiple isotopes could be distinguished and thus differentiated in one scan. PET imaging makes use of radioisotopes following a β^+-decay. After a short distance, the respective positron will stop and annihilate with an electron from the patient's tissue. Thereafter, two photons (0.511 MeV) will be emitted in opposite directions (approx. 180°). Despite the fact that PET is often referred to as superior compared to SPECT, the number of SPECT

examinations has remained stable or even increased in recent years [1], which underlines the continued importance of this technique.

In the following sections an overview of the fundamentals of nuclear medicine imaging, focusing on single photon emission imaging, will be given.

In general, the compiled physical principles about radioactivity and system configuration are based on the book "Emission tomography: the fundamentals of PET and SPECT" by M. N. Wernick and J. N. Aarsvold (2004) [34], and the published review "SPECT detectors: the Anger Camera and beyond" by T. E. Peterson and L. R. Furenlid (2011) [35].

1.2. Theoretical Background of Molecular Imaging

1.2.1. Photon Emission

Radioactive decay is a gradual process, where each decay can be assigned to one of the following two groups: isomeric and isobaric transitions [36]. Most radioisotopes start with an isobaric transition like alpha or beta decay, which then can result in an excited daughter radionuclide. The consequence to reach a more stable state is to release energy in the form of photons, the so-called gamma decay. Respective photons are emitted isotropically with unique characterizing energy for each radioisotope. This process is part of isomeric transitions as the atomic number keeps unchanged.

The transition energy ΔE results in the kinetic energy of the emitted photon and is the difference between the maternal (E_m) and the daughter (E_d) energy state ($\Delta E = E_m - E_d$). As an example, in the following the nuclear equation for the commonly used radioisotope ^{99m}Tc is displayed:

$$^{99m}_{43}Tc \xrightarrow{6.01\,h} {}^{99}_{43}Tc + {}^{0}_{0}\gamma \tag{1}$$
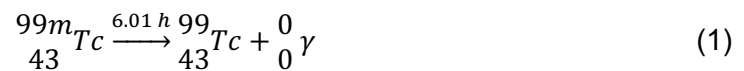
In general, each radioactive decay is a random event. Looking at the photons detected it needs to be considered that photon emission, as well as detection, follow the Poisson distribution. This means that one can only predict with a certain likelihood the number of decays since all individual disintegrations take place completely independently of each other. What nevertheless always applies is that the number of decays dN over a certain time dt is proportional to the absolute number of existing atoms N of the corresponding radioisotope:

4

$$-\frac{dN}{dt} \sim N \qquad (2)$$

If one integrates a decay constant λ characteristic for each radioisotope as $\frac{\ln 2}{t_{1/2}}$, one obtains the following regularity:

$$\frac{dN}{dt} = -\lambda N \qquad (3)$$

Radioactive decay as a function of time can then be easily described by the formula below. $N(t)$ describes the number of the remaining atoms at the time t, N_0 the amount for $t = 0$:

$$N(t) = N_0 e^{-\lambda t} \qquad (4)$$

To describe the totality of all occurred decays N_{decay} and thus the maximum number of decays to be detected between time t_1 and t_2, the following integral can be formed. The basal activity A_o is defined as the number of decays per second of a certain radionuclide for $t = 0$.

$$N_{decay} = \int_{t_1}^{t_2} A_o e^{-\lambda t} dt \qquad (5)$$

Finally, it should be noted that only a certain fraction of the decays that occur are registered by a specific system, e.g., a SPECT. Consequently, considering the sensitivity *sen* of the respective system, the following equation is obtained, which describes the sum of all detected decays $N_{registered}$:

$$N_{registered} = \int_{t_1}^{t_2} sen\, A_o e^{-\lambda t} dt \qquad (6)$$

1.2.2. Photon Detection

To derive added value from single photon emission imaging from a medical perspective, it is crucial to narrow down the point of origin as precisely as possible and accordingly, the location where the radiopharmaceutical has accumulated. For this purpose, two steps are required.
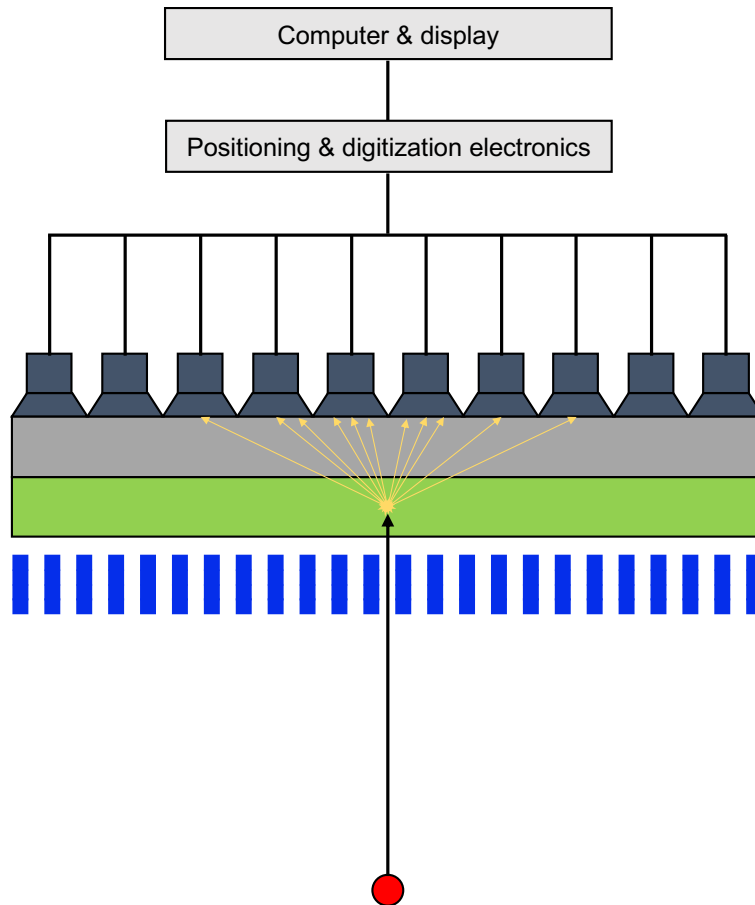
Figure 1: Gamma camera construction scheme.

This picture illustrates the general configuration of a gamma camera. The blue blocks represent a collimator, in this case with a parallel hole design for simplicity. The green rectangle is the scintillation crystal, which is connected to the dark gray array of photomultiplier tubes (PMTs) via the light grey colored light guide. The dot represents a photon with a corresponding line of response (LOR) shown as the black arrow reaching the scintillation crystal, and producing a light flash, shown as a yellow explosion symbol. Then, new photons, shown as yellow arrows, are detected by the PMTs as an electric current, which is then translated into a corresponding position and digitized for further analysis (for simplicity added as gray-colored boxes). Own illustration based on "CHAPTER 7 - Single-Photon Emission Computed Tomography," by G. L. Zeng et al., in *Emission Tomography*, M. N. Wernick and J. N. Aarsvold Eds. San Diego: Academic Press, 2004, pp. 127-152 [37].

Before photons will reach the detector, they need to overcome a collimator. This is mainly a plate made from metal with high atomic numbers, like tungsten, lead, or gold, with a certain thickness and multiple perpendicular boreholes. This leads to cone-shaped volumes of acceptance, from which photons can emerge to pass the holes without interactions and reach the detector as others will be absorbed. The second step is the actual detection process, which is made possible by a combination of a scintillation crystal, photomultiplier tubes (PMT), and electronics for processing and digitization [37]. The general construction of a gamma camera is illustrated in **Figure 1**.

For determining the information about the photon's point of origin, collimators and detection location are used to define the line of response (LOR) which is unique and goes through the imaged object. The collimator ensures that the fraction of emitted photons that do not follow the LOR are not able to reach the detector and thus, are not registered. In contrast, photons that follow the LOR can pass the collimator, reach the detector, and can then be detected by the system.

The detection process itself is based on scintillation, in which a scintillation crystal, usually made of thallium-doped sodium iodide [chemical formula: NaI(Tl)], is connected to an array of PMTs via a light guide [38]. Looking at the photons of the established ^{99m}Tc with a photon energy of 140.5 keV, the interaction with the crystal is mainly based on photoelectric absorption and Compton scattering. This means that the energy of the gamma rays is completely or to a certain extent transferred to a bound atomic electron which is thus put into an excited state. Scintillation crystals have an electronic band structure providing a valence and a conduction band in the crystal's lattice so that only defined energy states of the electrons are allowed. Single or multiple collision processes of the high-energetic gamma photons with the crystal's atoms lead to the excitation of electrons and a respective transfer from the valence band to the conduction band. This results in a positive hole in the valence and a negatively charged conduction band. After a short period of time, conduction electrons reintegrate into the valence band, resulting in a corresponding release of low-energy light. For further processing by the connected PMTs, it is essential to shift the emitted photons into the range of visible light. This is achieved by the addition of a certain impurity factor, in the case of NaI in form of thallium. To prevent absorption the fraction of thallium is kept very low, usually at around 0.1 mol% [35]. Like this, the luminescent efficiency is improved, and the wavelength of the scintillation photons is increased as electrons are now enabled to make a stop in the luminescent centers located in between both bands. As the recombination of electrons

7

from the luminescent centers leads to lower energy release, the photons' wavelength is increased and thus shifted into the visible range.

Next, these emitted flashes of lightning need to be converted and amplified. Hence, arrays of PMTs are connected via a light guide to the scintillator. First, the respective scintillation photons hit a photocathode where electrons, so-called photoelectrons, are ejected. Using a focusing electrode, the primary electrons are directed to an electron multiplier where electrons are hitting multiple diodes until a current from the initial photocathode to the final anode is measurable. Therefore, usually, an acceleration voltage of 100 V is applied [39, 40]. Finally, electronics and computational resources connected to the PMTs will convert the generated current pulse and calculate the time, position, and energy of each detected photon. (For a more in-depth explanation of scintillators and photodetectors, refer to Wilkinson (2004) [41] and Pichler and Ziegler (2004) [42].)

1.2.3. Collimation

The following general overview of this subject is based on Moore et al. [43], Van Audenhaege et al. [44], Meikle et al. [45], and Gunter [46].

As already mentioned, the challenge of single photon emission tomography is to create the LOR and besides the detection location, a second reference point is essential which is provided by the collimation process. A collimator is made of materials with high atomic numbers, such as tungsten, lead, or gold, and high density, which reduces penetration by randomly emitted photons not following the LOR and makes sure that only the desired photons following the LOR through the collimator's holes can reach the detector. These specific photons make up only a very small proportion (10^{-4} to 10^{-2}) resulting in rather poor sensitivity [44]. There are various collimator designs, which are briefly outlined in the following section (see **Figure 2**).
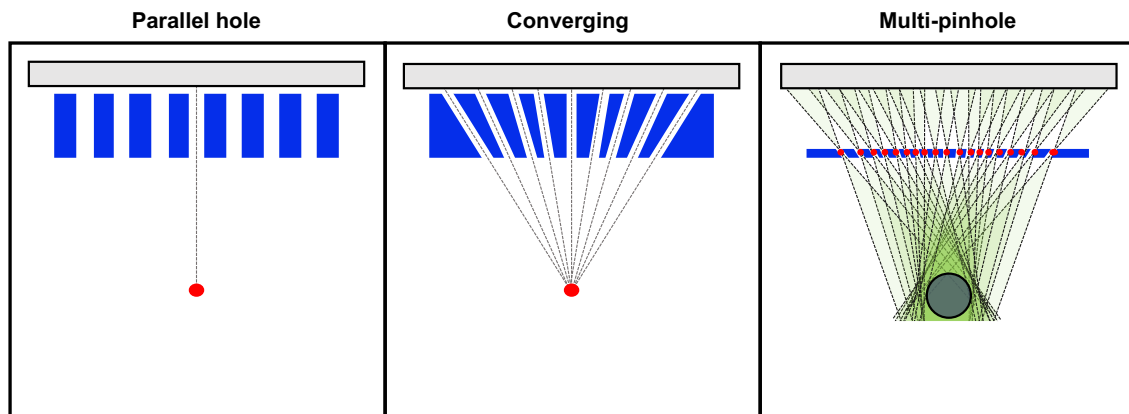
Parallel hole	Converging	Multi-pinhole

Figure 2: Design types of collimators.

This image illustrates the basic effect of the three most common collimator designs. The red dots stand for the corresponding focal points. Respective collimator is colored blue, and the grey rectangles represent the detector. For the scheme of the multi-pinhole configuration, a grey circle representing the imaged object was added. The green triangular shapes represent the respective fields of view (FOV) of the individual pinholes. Own illustration based on "CHAPTER 7 - Single-Photon Emission Computed Tomography," by G. L. Zeng et al., in *Emission Tomography*, M. N. Wernick and J. N. Aarsvold Eds. San Diego: Academic Press, 2004, pp. 127-152 [37].

In clinical practice, mainly **parallel hole collimators** are standard [47]. These collimators provide a honeycomb-like arrangement of parallel, mostly hexagonal holes, which are separated in between by lead. Consequently, each hole defines a cone-shaped volume where photons can originate to fully pass through these holes to reach the system's detector. According to the photon energies of the applied radioisotopes, the collimator's wall thickness needs to be adapted. In principle, higher photon energies ask for thicker septa in collimators to reduce septal penetration [44]. Further, the modification of the wall thickness as well as of borehole diameters may improve the system's resolution (thicker collimator, smaller borehole diameters) or sensitivity (thinner collimator, bigger borehole diameters). In general, to increase one of the two parameters the other one will be reduced, which is called the resolution-sensitivity trade-off. For imaging objects smaller than the system's detector size **converging hole collimators** are under investigation. For instance, to maximize the region of interest (ROI) on the detector and hence the intrinsic spatial resolution cone- or fan-beam collimators were developed. Respective holes are converging in the transverse as well as axial direction for the cone-shaped or only in the transverse plane for the fan-shaped collimators, where holes are parallel in the axial direction. In contrast, diverging collimators may be interesting in the future for dynamic scans, as large FOVs are necessary [48]. Another approach is **single- or multi-**

pinhole collimators. In this case, small pinholes are used instead of the holes mentioned above. Through these apertures, objects are projected onto the detector and are magnified, as illustrated in **Figure 3**. This design is commonly used for imaging small organs and animals, respectively, as it enables submillimeter spatial resolution without too high of a loss in sensitivity due to a bigger-sized detector [49-53]. In clinical practice, multi-pinhole collimators are also increasingly applied for cardiac [54-56], and brain SPECT [57, 58] for example.
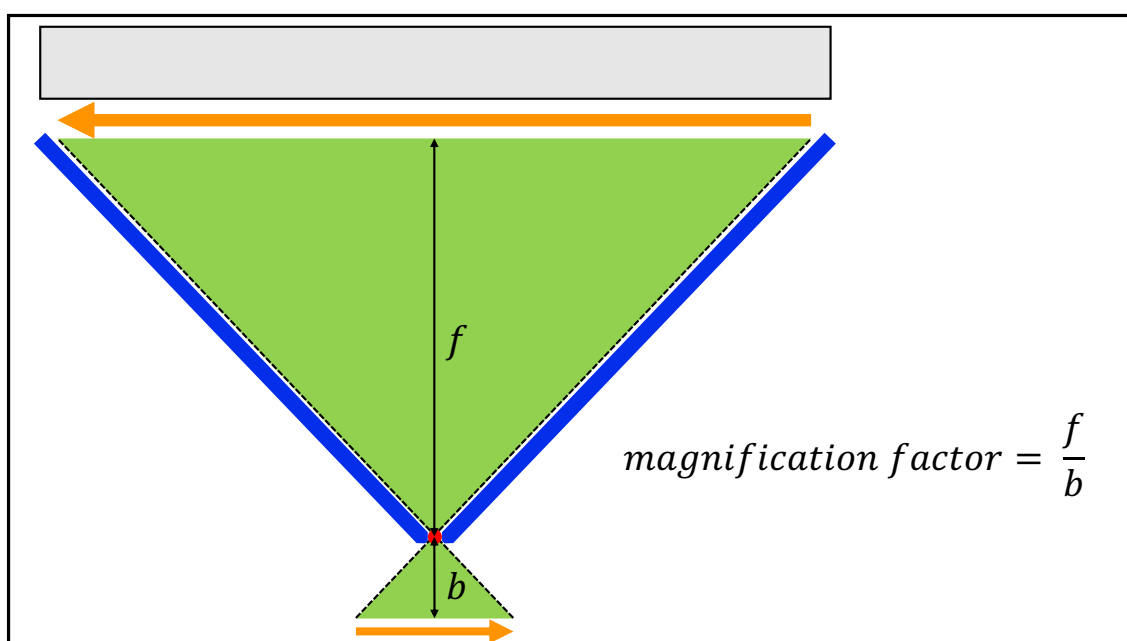

$$magnification\ factor = \frac{f}{b}$$

Figure 3: Simplified scheme of pinhole collimation geometry.

This picture exemplifies the physics behind pinhole collimators, here colored blue. The imaged object, represented by the orange arrow, with the distance b to the focal point (red circle), is projected mirrored on the detector (light grey rectangle). f corresponds to its distance to the focal point. This results in magnification by the factor $\frac{f}{b}$, when $b < f$. Own illustration based on "CHAPTER 7 - Single-Photon Emission Computed Tomography," by G. L. Zeng et al., in *Emission Tomography*, M. N. Wernick and J. N. Aarsvold Eds. San Diego: Academic Press, 2004, pp. 127-152 [37].

1.3. Single Photon Emission Imaging

Using single gamma rays for imaging in nuclear medicine is well-established and has a long tradition. It was first applied in 1958 by H. O. Anger as a device to image photon emission was built [59]. Even though many years have passed and there were made several advances in imaging techniques and system construction, the different ways of

single photon emission imaging still rely on an adaption of the so-called Anger camera [37].

1.3.1. The Gamma Camera

First, the general idea of a conventional gamma camera will be outlined. The main components include the collimator, the scintillator, an array of connected PMTs, and further electronics for calculation and digitization to then export the data to a computer. Collimation of incoming photons is required to ensure that only a certain fraction of photons reaching the collimators perpendicularly are allowed to reach the detector undisturbed. To make sure that other photons will be absorbed, these parts are usually made from elements with high atomic numbers like gold, tungsten, or lead [43, 44].

Next, the photons that could pass undisturbed are reaching the scintillator which works like a wavelength shifter. There will be some photons that pass through without any interaction, but then there will be photons that will be absorbed by the scintillator. Consequently, a visible light flash will be created. As a scintillator is usually as transparent as possible for long wavelengths, the new photons can thus strike the PMTs which are connected through an optically transparent light guide.

In this step, at first, the photons are hitting the photocathode. Based on photoelectric absorption, photoelectrons are released from the material. Then, these photoelectrons are accelerated by a certain voltage and hit multiple dynodes leading to a generation of secondary electrons. As a result, a certain current will be measurable. The measured current of all PMTs together which is due to an interaction in the scintillator is proportional to the total energy of the original photon.

Electronics connected to the PMTs are then processing the registered activities and extracting the information about the location on the detector and the energy of the photon. All this data is digitized and then stored on a computer so that images can be reconstructed [37].

1.3.2. Planar Single Photon Emission Imaging

The simplest way of implementing a gamma camera in the field of medical imaging is planar imaging. Therefore, the position of the detection interface is kept stationary, and all the information of the investigated patient will be registered from this one single view. Hence, the registered activity can only be stored as projections from this one view, and

distribution is depicted as an overlay, which means that a defined localization is only possible two-dimensionally.

1.3.3. Single Photon Emission Computed Tomography

To decode the third dimension, projections from multiple angles need to be registered. Therefore, dedicated systems to enable emission tomography based on gamma cameras were built [60, 61]. Usually, one or two detector heads are mounted to a gantry centered around the patient. While photons are detected, the gamma cameras will rotate incrementally to collect data from multiple detection angles. After the acquisition, this allows for displaying the radioisotope distribution in the patient either as two-dimensional (2D) slices or as three-dimensional (3D) volumes.

1.3.4. SPECT/CT

Finally, hybrid imaging was established, where SPECT systems were extended by a CT component for co-registration of the patient's anatomy [18]. This enables the assessment of the anatomic correlation of a certain radioisotope uptake. Further CT data can be used to calculate attenuation factors of tissues which then can be integrated into the reconstruction of the SPECT data [62, 63]. Usually, the CT component is added to a separate gantry behind the SPECT system. This means, that the patient needs to be moved after finishing the SPECT acquisition to the FOV of the CT. In the following, both tomographic images acquired are co-registered which then allows for accurate correlation of anatomical and functional information obtained. The advantages of attenuation correction and improved evaluation of the images lead to better diagnosability and hence the number of clinical applications for SPECT/CT is constantly rising [30, 64].

1.4. Tracer: 99m-Technetium

For single photon emission imaging, it is essential to use radioisotopes that reliably follow gamma decay and emit photons of a well-usable energy spectrum. With a half-life of 6.0072 hours and photon energy of 140.5 keV, ^{99m}Tc combines these requirements well and is, therefore, the most widely used radioisotope clinically and preclinically [65, 66], with 30 to 40 million examinations per year worldwide [67]. Although a short half-life is beneficial for the use in patients as radiation dosage is kept low, it poses a challenge in

production and especially in logistics [68]. Hence, not ^{99m}Tc but its maternal radioisotope 99-molybdenum (^{99}Mo) with its half-life of 66 hours is used for delivery to the facilities. There, it then will be eluted as ^{99m}Tc. ^{99}Mo is produced primarily by using highly enriched 235-uranium (^{235}U) targets in nuclear reactors that are irradiated with neutrons, producing ^{99}Mo as a fission product [69]. In the following, ^{99m}Tc-generators based on column chromatography containing the maternal nuclide adsorbed as ammonium molybdate [$(NH_4)_2MoO_4$] by aluminum oxide (Al_2O_3) will be constructed. To enable easy transportation in the following, radiation shielding will be added. At the medical facility, the next step will be the elution process to receive the required amount of ^{99m}Tc for respective examinations. As pertechnetate (^{99m}TcO$_4^-$) tends to bind less tightly to the chromatographic band because of its single negative charge, pharmaceutical grade saline (NaCl) is used as the eluent leading to Na(^{99m}TcO$_4$) as the desired eluate. At the same time, none of the maternal nuclide in the form of MoO$_4^{2-}$ is eluted because it is more strongly bound to Al_2O_3 due to the double negative charge. The eluted amount of ^{99m}TcO$_4^-$ may then be used purely or labeled to a specific radiopharmaceutical for medical examination [68].
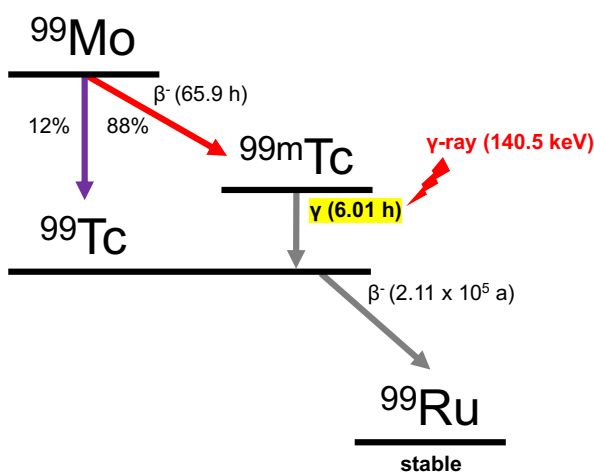
Figure 4: Decay scheme of ^{99}Mo.

The values in brackets in black letters indicate the half-lives $t_{1/2}$ of the corresponding isotopes with the decay type added before. The energy of the gamma rays was added in thick red letters. Own illustration based on *"2, Medical Isotope Production and Utilization" in Molybdenum-99 for medical imaging.* by the National Academies of Sciences Engineering and Medicine: Committee on State of Molybdenum-99 Production and Utilization and Progress Toward Eliminating Use of Highly Enriched Uranium, Washington, DC: National Academies Press, 2016 [70].

1.5. Reconstruction and Data Processing

1.5.1. Image Reconstruction

During the acquisition process, the computer creates a unique file listing the collected information of all registered counts, which are then stored in the form of a list-mode dataset. It contains all information of each scintillation event about location, time, and energy [71]. These data can then be used for image reconstruction, which will be briefly summarized. Based on the collected list-mode data, the information is converted to two-dimensional sinograms. Sinograms describe two-dimensional images with count location on the detector on the x-axis and the detector's angular position on the y-axis. These sinograms are plots of line integrals of an image function, which is referred to as the Radon transform. Consequently, the process of projection describes how to get from a certain 2D slice of the object to the corresponding unique sinogram. Accordingly, the goal is back projection of the registered sinogram to then reconstruct the 2D slices of the investigated object. Finally, the sum of all created slices can be merged into a 3D dataset of the object. The main problem is that a projection acquired with the detector at a certain angle does not provide information about the depth at which the gamma decay occurred. Hence, an infinite amount of images lead to the same projection. Therefore, multiple detection angles are required. By increasing the number of angular positions for data acquisition, the number of solutions resulting in the same projection decreases.

There are two different approaches to image reconstruction: analytical [72], and iterative methods [73]. In the past, analytical reconstruction, with its main representative, the filtered back projection (FBP) [74, 75], was used because of its acceptable results without high computational efforts. With the advancement of computers and their computational capabilities, the importance of iterative reconstruction algorithms, for instance, maximum-likelihood expectation-maximization (MLEM) [76], increased. Nowadays, in SPECT, analytical methods have been almost completely replaced by iterative algorithms in clinical and experimental practice [77]. These two approaches are briefly outlined in the following section.

In the **filtered back projection**, the registered sinograms are processed in two phases. First, the information is transformed according to the Fourier transform so that each element of the image corresponds to a specific frequency. To reduce the blur in the final reconstructed images, it is essential to filter these frequencies. Therefore, a weighted filter is applied that adds a certain weighting factor to the different frequencies contained in the data. Second, as the name suggests, FBP creates back projections of the collected

sinograms for each detector angle. In the absence of information about the depth of origin of the detected photons, the information is evenly distributed over the pixels corresponding to each sinogram. This is the reason for the resulting blur and therefore requires an additional filtering step as mentioned above.

The approach of **iterative methods** is to create an image estimate which is then compared to the true projection data detected. The information from the comparison is then implied and helps to create a new and more accurate estimate. This process is called iteration (*it*). Theoretically, it then takes an infinite number of iterations to obtain the correct image that represents the investigated object. To reduce computational expense, collected 3D data is converted into 2D data, called rebinning, so that the reconstruction also yields only 2D data, but these can be merged into 3D images after reconstruction [78]. The goal of the established maximum-likelihood expectation-maximization is to calculate a solution with the highest likelihood to create the measured sinogram registered by the detector. Therefore, the distribution of detected counts is described using the Poisson law. This algorithm may also be divided into two phases. The expectation is the first, where an estimate is created defining the likelihood of possible reconstructed images using the measured data. In the following maximization is performed to find the image with the highest possible likelihood of creating the measured data. In each iteration, the current estimates are converted to simulated projections which are then compared to the measured projections. The result of the comparison is implemented, and a new estimate is generated. As each *it* contains creating the projection and back projection, the process is computationally intensive and takes time. To enhance the effectiveness, acceleration techniques, like ordered subset expectation maximization (OSEM) [79], were developed. This algorithm divides the collected data into multiple subsets (*sb*) to reduce the computational effort for each iteration without comprising image quality. Further adaptations of the OSEM algorithm for small-animal SPECT with multi-pinhole collimation were made, as some susceptibility to inaccuracies was shown for OSEM here [80]. The pixel-based ordered subset expectation maximization (POSEM) divides the collected data into *sb* while using pixels to which the projections are evenly distributed. Like this inaccuracies were reduced and reconstruction speed was improved [80]. Another progress was the similarity-regulated OSEM (SROSEM) introduced by Vaissier et al. [81]. Here, the similarity of update factors for each reconstructed voxel is compared to the MLEM update factors until a certain predefined percentage is reached. Therefore, 1 *it* of MLEM is performed in the beginning to calculate corresponding update factors for each voxel so that the percentage

deviations of the SROSEM *sb*s can be compared. This is necessary as its predecessor algorithms struggle to achieve accurate results for data with high background noise. SROSEM reduces the number of updates (*NoU*) if voxels become noisier because of a low number of counts to decrease reconstruction-caused artifacts as well as simultaneously shorten the reconstruction time. This leads to the possibility to use the same reconstruction setting for low- and high-count studies and only adjust the noise by post-reconstruction filtering as proposed by the authors [81].

1.5.2. Post-reconstruction Filtering

As stated above, iterative reconstructed data often result in noisy images and subsequently alter accurate interpretation. Hence, applying noise suppression filters to the reconstructed images is a common practice. These filters work as low-pass filters as they reduce the high frequencies of an image by a certain fraction. Since these high frequencies are also responsible for the sharp edges in an image, using such a filter always leads to a limitation of the maximum spatial resolution [82]. Therefore, certain functions describing a window with a defined cut-off frequency were defined. Frequency windows can either be shaped rectangular or be described as functions like Hanning or Gaussian. Since the Gaussian filter is supreme considering qualitative analysis, contrast as well as contrast-to-noise ratio, it was applied to the obtained images [83, 84].

1.6. Advantages of SPECT

The important role of SPECT in molecular imaging is easily understood as it provides many characteristic advantages compared to its competitor PET. Since radioisotopes used for SPECT have significantly longer half-lives (e.g., ^{99m}Tc: 6.01 h; ^{123}I: 13.2 h; ^{201}Tl: 3.05 d) compared to radionuclides for PET (e.g., ^{18}F: 109.7 min; ^{11}C: 20.4 min) it is not necessary to produce the tracers directly onsite by a cyclotron. This improves the accessibility of SPECT in two ways, allowing the establishment of SPECT imaging facilities in peripheral hospitals to which radioisotopes can be distributed and reducing the overall financial burden. Further, these longer half-lives allow dynamic studies for slow metabolic processes [85]. In terms of maximum spatial resolution, PET is usually superior to SPECT in the clinical setting. However, considering that this limitation of SPECT is only a problem of impaired count rate due to lower system sensitivity and thus a technical problem, the potential of SPECT can be recognized. With the advances in multi-pinhole collimation, detector materials as well as reconstruction algorithms,

submillimeter spatial resolution is realistically achievable as published in preclinical circumstances [86-89]. Moreover, as radioisotopes emit gamma rays with unique photon energy, simultaneous imaging of multiple radioisotopes applied is theoretically possible and under investigation [90].

1.7. Special Features of Small-animal SPECT

Looking at preclinical research using small rodents, molecular imaging is a challenge as it was first introduced for imaging humans. Therefore, to make use of SPECT imaging preclinically, it was vital to improve spatial resolution without significantly limiting the system's sensitivity. This is important to keep the administered doses of radioisotopes as low as possible, especially to avoid unnecessary harm to animals. Therefore, unique improvements were made to dedicated small-animal SPECT systems. For instance, the two investigated systems are based on using large stationary detectors with a fixed FOV and a movable bed for small rodents to change the volume that will be scanned in the FOV (cf. **Figure 5**). This configuration leads to several advantages. Like this, maintenance is kept simple and can be performed more easily, there are less prone parts that could affect the scanning accuracy. And lastly, as no detector head needs to be moved, for dynamic scans frame lengths can be extremely short [49, 87].

Different modifications were performed to address these challenges. Some examples will be described briefly. One approach taken by *MILabs B.V.* is the combination of either two or three stationary detectors, a moveable XYZ-stage in which the small rodents are placed, and multi-pinhole collimation with a fixed central FOV. Due to pinhole collimation, high magnification factors lead to increased system spatial resolution despite the lower intrinsic spatial resolution of the detectors. Hence, using large detectors, established for clinical use, with an intrinsic resolution of only 2 to 4 mm, submillimeter system spatial resolution is made possible by magnification [87]. Further, dedicated reconstruction algorithms were introduced which then use all the registered projections to reconstruct the entire volume of interest. This is necessary as the FOV is too small to perform a total-body scan. This method is called the scanning focus method (SFM) [88]. Other manufacturers, for example, *Bioscan* with the NanoSPECT-NSO and *GE Healthcare* with the X-SPECT, focus on a design with rotating detector heads. To reduce scanning time and increase sensitivity these systems provide four detector heads mounted to a gantry instead of the usual two-headed configuration. Further, the advancement in semiconductor detectors made for instance from cadmium zinc telluride (CZT), in the

case of the NanoSPECT-NSO, enables the direct conversion of registered photons into an electrical signal. PMTs are not needed anymore, which results in a more reliable and resistant detector with higher energy and intrinsic spatial resolution as well as detector sensitivity [91]. Moreover, some systems like the NanoSPECT/CT[PLUS] from *Mediso* use multiplexed multi-pinhole collimators, which means, that the projections registered overlap each other to increase the system's sensitivity even further [53, 92-94].
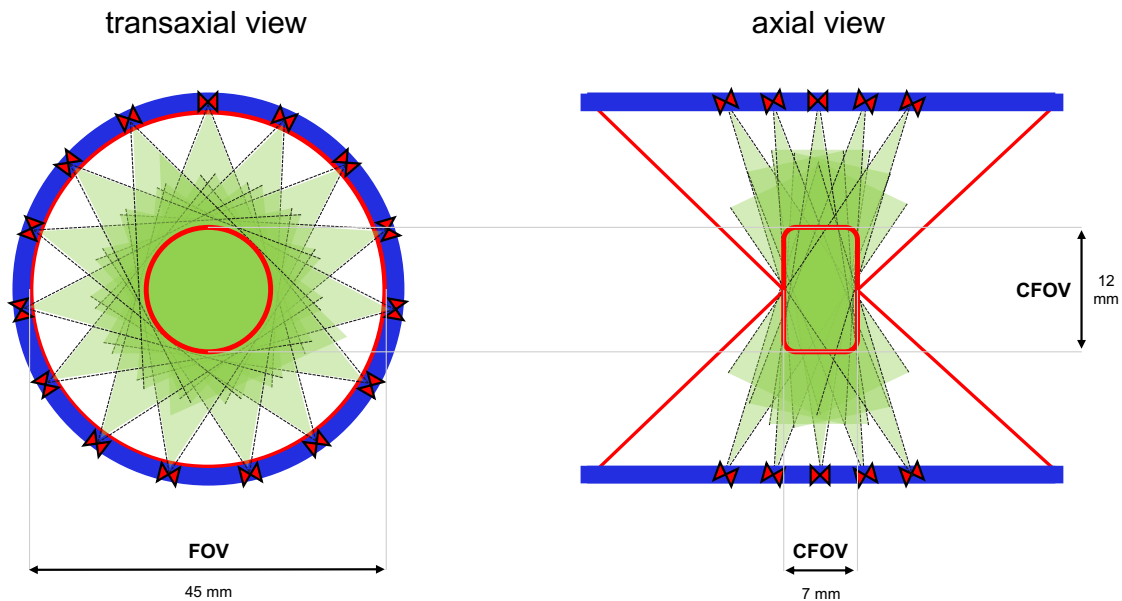

Figure 5: Alignment of the fixed field of view in the U-SPECT[5]/CT E-Class.

The multi-pinhole collimator is shown in blue, with the pinholes represented by the red hourglass shapes pointing to the center. The green triangles represent the individual fields of view (FOV) of each pinhole, which in aggregate generate the central field of view (CFOV) marked by the red circle in the transaxial view and the red rectangle in the axial view. The CFOV measures 12 mm in diameter and 7 mm in length. The collimators cover a full FOV of 45 mm in diameter. Own illustration based on *"Targeted multi-pinhole SPECT,"* by W. Branderhorst et al., 2011, Eur J Nucl Med Mol Imaging, vol. 38, no. 3, pp. 552-61 [95].

1.8. Performance Standards for SPECT

The assessment of performance characteristics is mainly defined in the document "*Performance Measurements of Scintillation Cameras NU-1-2018*" published by the *National Electrical Manufacturers Association* (NEMA) [96]. This guideline provides exact procedures to measure the system's spatial resolution, uniformity, energy resolution, and count-rate performance, to name some examples. NEMA standards are

provided to ensure that measurements are performed under reproducible circumstances and consequently different systems' performances can then be compared. As NEMA has published standards for clinical gamma cameras as well as PET systems for clinical use, only small-animal PET systems were addressed with the standard NU-4-2008 [97]. Looking at small-animal SPECT, the challenge is, that the defined standards of NU-1-2018 are not directly transferable to multi-pinhole SPECT imaging [96]. Consequently, the methodology of this study is mainly based on the published papers of the predecessors of U-SPECT[5], since there were no major changes in the general configuration of the system [5, 49, 87, 88].

2. Aim of the Thesis

The progress in system design of preclinical SPECT/CT with stationary detectors and multi-pinhole collimation has shown that submillimeter high spatial resolution in combination with adequate sensitivity can be achieved. Therefore, micro-SPECT/CT has become a powerful imaging tool in research with small rodents. It is crucial to assess the individual performance of a new system based on phantom measurements. Especially for upcoming research projects with this system, it is important to plan the imaging protocols in such a way that good image quality can be obtained, and the expected spatial resolution can also be narrowed down. Particularly with respect to the reduced detection area, it will be important to see if the advances in sensitivity and spatial resolution for future in vivo small animal experiments can be sustained for this system.

The goals of my work have been as follows:

A. To evaluate the maximum achievable performance values sensitivity, spatial resolution, and uniformity.
B. To determine the advantages and optimal reconstruction parameters of the recently published iterative SROSEM algorithm based on image quality.
C. To apply a recent template-based analysis of the contrast-to-noise ratio of tomographic images as an indicator for image quality.
D. To contrast the two-headed system with its proven predecessor with three detectors in terms of sensitivity, spatial resolution, uniformity, and image quality.
E. To compare different amounts of activity concentrations representing different count levels as a function of contrast-to-noise ratio and spatial resolution with the goal of translating theoretical performance to expected performance in animal studies.

3. Materials and Methods

3.1. Small-animal SPECT Systems

3.1.1. 2-Detector-Scanner (U-SPECT^5/CT E-Class)

The dedicated small-animal U-SPECT^5/CT E-Class (*MILabs B.V.*, Utrecht, The Netherlands) located at the *Comprehensive Heart Failure Center (CHFC)*, Würzburg, Germany (**Figure 6**) was primarily investigated with respect to the performance of the SPECT component. The system consists of two stationary scintillation detectors (59.5 cm by 47.2 cm) made of thallium-doped sodium iodide [chemical formula: NaI(Tl)] crystals with a thickness of 9.5 mm optically connected to an array of PMTs, giving a total detection surface of 5616.8 cm^2. The energy resolution provided by these detectors is smaller than 10% for 140 keV photons [93, 98]. For the fully equipped U-SPECT^5 model an additional third bottom detector is added (**Figure 7**). The overall construction is comparable to the previous generation U-SPECT systems (U-SPECT$^+$ and U-SPECT-II, *MILabs B.V.*) [5, 49]. As the detector segments connected to each PMT are nonoverlapping, this leads to a breakdown into individual smaller gamma cameras [99]. Electronics connected to the PMTs digitize the registered information about detected photons, which are then transferred via a wired gigabit Ethernet connection to the acquisition workstation [49]. The system provides interchangeable tube-shaped multi-pinhole collimators for different purposes with a fixed FOV (cf. section **3.2**). An animal bed mounted on a movable XYZ-stage allows different areas of the examined object or animal to be placed in the central field of view (CFOV). This takes the form of a spiral step mode so the acquired data can be merged, enabling both focused scans and total-body scans of objects larger than the CFOV [88, 95, 100]. The area to be imaged can be defined in advance, as previously described by Branderhorst et al. [95], by selecting the scan volume based on webcam or X-ray images. After defining the intended scan volume, the number of bed positions with the corresponding acquisition time for each position as well as the effective scan time is calculated automatically.
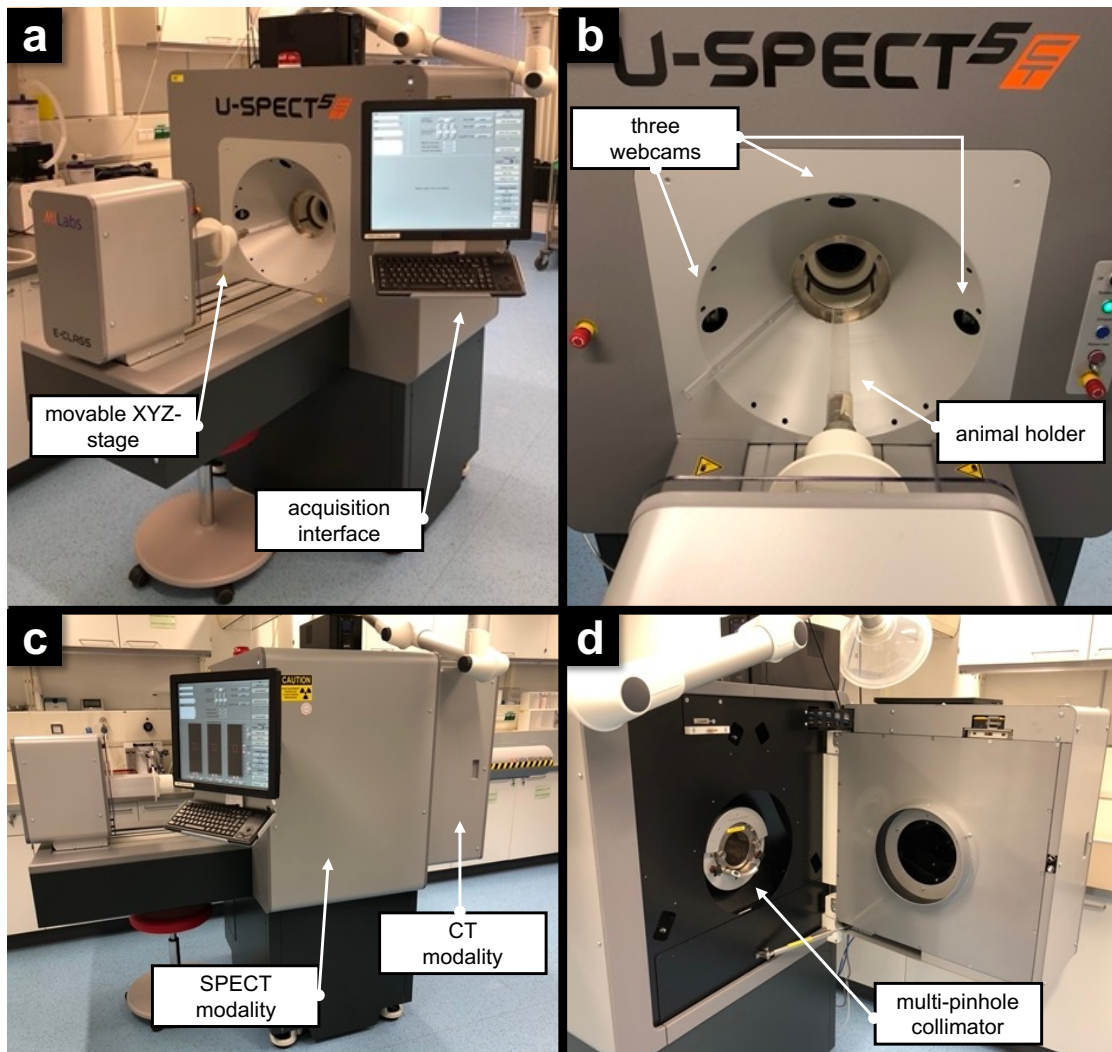
Figure 6: Investigated two-headed small-animal SPECT (U-SPECT[5]/CT E-Class).

In (**a**) the system is shown from the front. The housing of the micro-SPECT modality can be seen with the moveable XYZ-stage in the foreground. (**b**) The animal holder in which the examined phantoms were placed is attached to the XYZ-stage. Three webcams can be used to define the scanning volume in three dimensions. (**c**) The CT gantry is located behind the SPECT modality. (**d**) The SPECT gantry is accessible from the rear to exchange the multi-pinhole collimators.
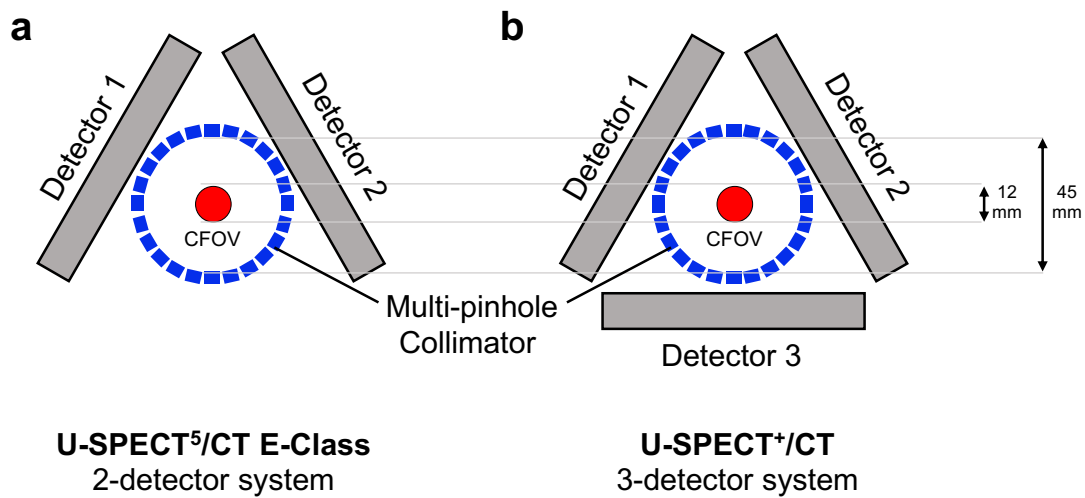
a

Detector 1
Detector 2

CFOV

Multi-pinhole
Collimator

U-SPECT⁵/CT E-Class
2-detector system

b

Detector 1
Detector 2

CFOV

Detector 3

12 mm
45 mm

U-SPECT⁺/CT
3-detector system

Figure 7: Simplified illustration of the configuration of the detectors for the two-detector system (**a**) and the conventional three-detector system (**b**).

The detectors, represented as grey rectangles, are stationary and arranged triangularly. As shown, no bottom detector was added for the U-SPECT⁵/CT E-Class system. Each detector, made of 9.5 mm thick thallium-doped sodium iodide [NaI(Tl)] crystals, measures 47.2 cm by 59.5 cm. The 75 pinholes of the exchangeable tube-shaped multi-pinhole collimators, here colored blue, are all directed to the central field of view (CFOV). The collimators' tube diameter is 45.0 mm and the size of the CFOV is 12.0 mm in diameter and 7.0 mm in length. Adapted from "Performance evaluation of fifth-generation ultra-high-resolution SPECT system with two stationary detectors and multi-pinhole imaging," by J. V. Hoffmann et al., 2020, EJNMMI Phys, vol. 7, no. 1, pp. 1-15, Art no. 64 [31].

3.1.2. 3-Detector-Scanner (U-SPECT⁺/CT)

The U-SPECT⁺/CT (*MILabs B.V.*) at the *Advanced Science Research Center*, Kanazawa, Japan, has an analogous system design to its successor in terms of construction, data acquisition process, and collimator configuration (**Figure 8**). The related SPECT modality is integrated into the versatile emission computed tomography (VECTor) platform for simultaneous SPECT and PET imaging [6]. The main difference is the added third bottom detector, i.e., three stationary detectors, each measuring 59.5 cm x 47.2 cm, with 9.5 mm thick NaI(Tl) crystals, giving a total detection area of 8425.2 cm^2 covering the entire 360° around the FOV [5].
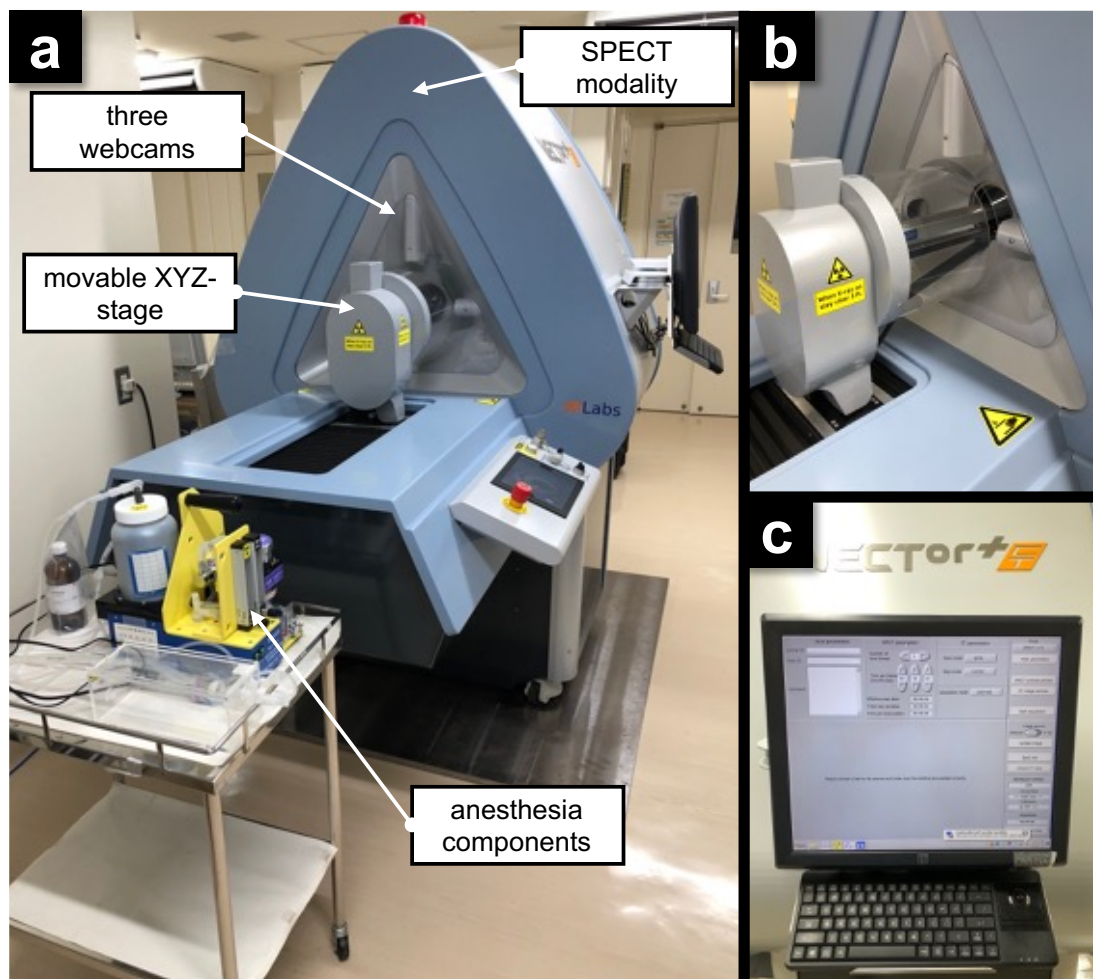
Figure 8: Small-animal SPECT scanner with three detectors (U-SPECT+/CT) used for comparison.

(**a**) Image of the U-SPECT$^+$/CT with three detectors. The object or animal is placed in a holder mounted to the XYZ-stage, which allows different areas to be moved into the central field of view (CFOV) of the scanner. The three integrated webcams enable 3D image-based scan volume selection. (**b**) Close-up of the XYZ-stage and webcams. (**c**) Acquisition interface for defining scan parameters and image-based volume selection.

3.2. Investigated Collimators

Three different multi-pinhole collimators were investigated. They are all made from tungsten and have five rows of 15 pinholes focusing on a CFOV of 7 mm (axial) by 12 mm (transaxial). Hence, the scanning volume of one single bed position of the system corresponds to the size of the CFOV. All three collimators are manufactured by *MILabs B.V.* and are specifically designed for mouse imaging (cf. **Table 1**, **Figure 9**). Pinhole sizes vary from 0.25 mm for the XUHR-M (extra ultra-high resolution mouse imaging) to

0.60 mm for the GP-M (general purpose mouse imaging) to 1.00 mm for the UHS-M (ultra-high sensitivity mouse imaging). The pinholes of rows 1, 2, 4, and 5 are installed at an angle so that all pinholes are focused on a central scan volume defining the CFOV (cf. **Figure 5**). The inner diameter of collimators measures 45 mm. To prevent the projections deriving from different pinholes from overlapping, an outer shielding made of lead was applied [5].

Collimator type	XUHR-M	GP-M	UHS-M
Purpose	Extra ultra-high resolution mouse imaging	General purpose mouse imaging	Ultra-high sensitivity mouse imaging
Pinhole size [mm]	0.25	0.60	1.00
Number of pinholes		75	
Inner diameter [mm]		45	
Central field of view - length [mm]		7	
Central field of view - diameter [mm]		12	

Table 1: Specifications of the used collimators.

Adapted from *"Performance evaluation of fifth-generation ultra-high-resolution SPECT system with two stationary detectors and multi-pinhole imaging,"* by J. V. Hoffmann et al*., 2020, EJNMMI Phys*, vol. 7, no. 1, pp. 1-15, Art no. 64 [31].
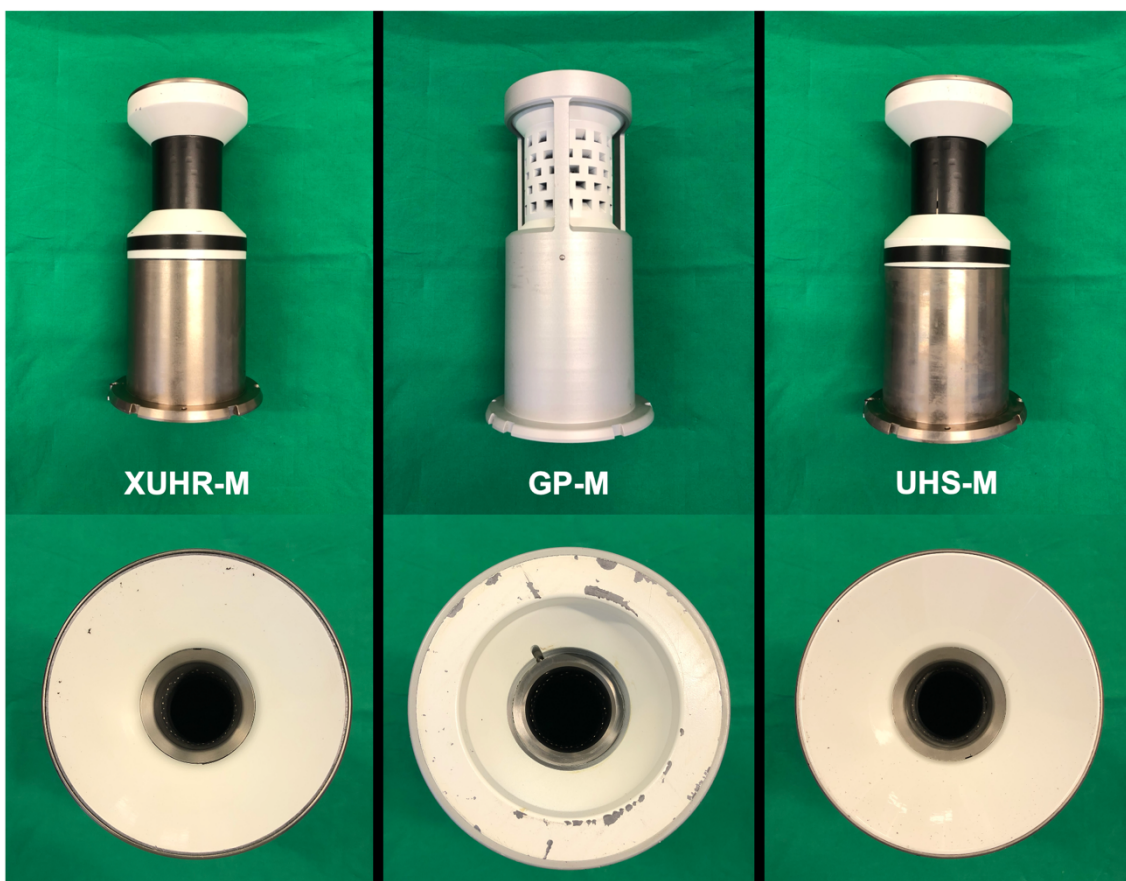
Figure 9: Investigated collimators for dedicated mouse imaging.

The images of the collimators examined are described from left to right: the first is for extra ultra-high resolution mouse imaging (XUHR-M) with 0.25 mm pinhole diameter, the middle one with 0.60 mm pinholes is for general purpose mouse imaging (GP-M), and the ultra-high sensitivity mouse imaging collimator (UHS-M) with pinholes of 1.00 mm diameter is shown on the right. The inner diameter of all three collimators measures 45 mm.

3.3. Specifications of Used Phantoms

Mini Derenzo Phantoms

For assessing spatial resolution as well as contrast-to-noise ratio three different mini Derenzo phantoms (*Vanderwilt Techniques*, Boxtel, The Netherlands) were used. Corresponding inserts measure 12 mm in diameter and 8 mm in length for the 850.350 and 850.100 as well as 24 mm in diameter and 12 mm in length for the 850.500. For filling the capillaries of the corresponding insert completely, a volume of approximately 0.80 ml is required for the 850.500, 0.15 ml for the 850.100, and 0.10 ml for the 850.350. Each insert counts six different-sized capillary sectors. In each section of the same-sized capillaries, the distance in between equals the diameter of the corresponding hot rod

sector. For the smallest phantom 850.350 diameters range from 0.22 to 0.50 mm, for the mid-size 850.100 from 0.35 to 0.75 mm, and for the biggest mini Derenzo phantom 850.500 from 0.70 to 1.50 mm.
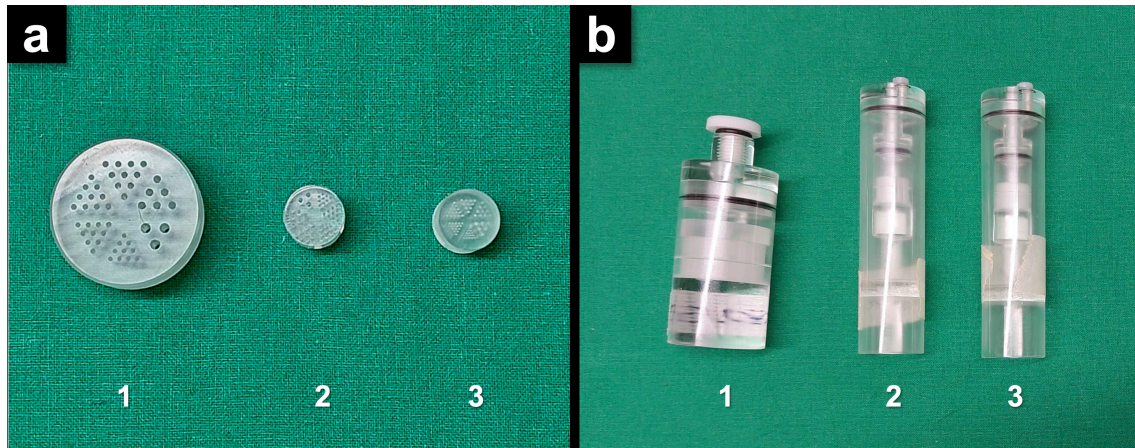

Figure 10: Inserts and respective cylindrical phantom holders of the three applied mini Derenzo phantoms.

The phantoms used consist of inserts with six rod sections of different diameters each (**a**). From left to right, the inserts of the 850.500 (**1**), rod range: 1.50-0.70 mm, 850.100 (**2**), rod range: 0.75-0.35 mm, and 850.350 (**3**) phantom, rod range: 0.50-0.22 mm, are shown. In (**b**) the corresponding cylindrical phantom holders are displayed of which the 850.100 holder was used for the uniformity measurements.

Uniformity Phantoms

The mini Derenzo phantom 850.100 described in the previous section was used as a uniformity phantom by removing the cylindrical insert. This results in a phantom with a cylindrically shaped volume of 13 mm in diameter and 10 mm in height, measured on the inside. Consequently, the respective chamber volume was 1.3 ml.

Phantom type	850.500	850.100	850.350
Purpose	Ultra-micro resolution phantom	Ultra-high micro resolution phantom	Ultra-high plus micro resolution phantom
Diameter of insert [mm]	24	12	12
Hight of insert [mm]	12	8	8
Diameter of hollow channels - range [mm]	0.70 - 1.50	0.35 - 0.75	0.22 - 0.50

Table 2: Specifications of the used mini Derenzo phantoms.

Adapted from *"Performance evaluation of fifth-generation ultra-high-resolution SPECT system with two stationary detectors and multi-pinhole imaging,"* by J. V. Hoffmann et al*., 2020, EJNMMI Phys*, vol. 7, no. 1, pp. 1-15, Art no. 64 [31].

3.4. Tracer

For all performed experiments ^{99m}Tc-pertechnetate (TcO$_4^-$) was used as the radioactive tracer as it is already established for performance studies [93, 101-104]. Therefore, a ^{99m}Tc-generator was used, which produces the metastable ^{99m}Tc from ^{99}Mo ($t_{1/2}$ = 65.924 h) [69, 105]. The subsequent decay to ^{99}Tc leads to gamma emission with a photon energy of 140.5 keV [106], and its half-life for gamma emission is 6.0072 hours [69, 105]. The tracer was provided by the *Department of Nuclear Medicine, University Hospital Würzburg*.

3.5. SPECT Imaging

3.5.1. Preparation of Tracer Solution

The different activity concentrations were measured using a dose calibrator (ISOMED 2010, *Nuvia Instruments*, Dresden, Germany). Daily quality control and background correction were performed as recommended by the manufacturer. For all measurements the applied activity concentrations were adjusted to the start of the acquisition by using the respective formula for decay correcting:

$$A_t = A_o \times e^{-\lambda t} \tag{7}$$

A_o describes the initial activity in [MBq], t the elapsed time, and A_t the activity at time t. λ is the decay constant, which is defined as $\lambda = \frac{\ln 2}{t_{1/2}}$, where $t_{1/2}$ is the half-life of the respective radioisotope, in this case, ^{99m}Tc.

3.5.2. Quality Control and Calibration

Based on the recommendations of *MILabs B.V.*, which are included in the corresponding user manual (Version 03.03) [98], quality control and calibration have been performed as follows. Monthly uniformity and resolution scans were performed for all three collimators of interest. Using the mini Derenzo phantoms described in paragraph **3.3**, it was confirmed that the system performs consistently for these two parameters. In addition, using a point source of ^{99m}Tc, calibration factors were determined and incorporated into the reconstruction software to allow the most accurate quantification from the reconstructed data.

3.5.3. Data Acquisition

U-SPECT^5 E-Class: Projections are registered in a list-mode format so that the required energy window can be defined after acquisition. For data acquisition, the dedicated software MILabs.Acq provided by the manufacturer was used (*MILabs B.V.*, Version 8.62). The acquisition was processed on an *Amplicon* workstation (*Amplicon Liveline LTD*, Brighton, UK, Model: 1538804 4917 C) equipped with an Intel® Core™ CPU i5-2400 (3.10 GHz) and installed memory of 4.00 GB. Thereafter, data is transferred to the dedicated workstation for reconstruction and post-reconstruction editing via a local area network.

U-SPECT$^+$: The acquisition process for the U-SPECT$^+$ followed the same procedure, also using the associated acquisition software MILabs.Acq (*MILabs B.V.*, Version: 3.9.4). The workstation used for this purpose was a Precision T1650 (*Dell Technologies*, Round Rock, TX, USA) containing an Intel® Xeon® CPU E3-1225 v2 (3.20 GHz) with 4.00 GB of RAM. This is followed by a wired transfer to the dedicated reconstruction computer via a local area network.

3.5.4. Image Reconstruction

U-SPECT[5] E-Class: Reconstruction of the registered list-mode datasets was performed by applying the SROSEM algorithm [81] as provided and recommended by the manufacturer. For this purpose, the special reconstruction software MILabs.Rec (version 8.06) was used on a Dell PowerEdge T630 server (*Dell Technologies*) equipped with two Intel® Xeon® E5-2690 v4 processors (2.6 GHz each) featuring 14-core DDR4 RAM with 128 GB RDIMM memory and an M60 Nvidia graphics card. As no standard in reconstruction settings exists and a sensitive adjustment of these is essential since both noise and contrast are affected [107], a structured analysis comparing the newly published SROSEM algorithm with its predecessor POSEM [80] and the established MLEM [108] algorithm was performed and respective explanation can be found in the following paragraph **3.5.5**. Taking this into account the datasets for this study were reconstructed using SROSEM with 3 *it* and 128 *sb* which also corresponds to the literature [81].

U-SPECT[+]: Since the SROSEM algorithm is not available in the previous generation U-SPECT[+], the comparative measurements were reconstructed in POSEM with the matching *NoU*, i.e., 384 (32 *sb*, 12 *it*). The reconstruction was performed on a PowerEdge T620 server (*Dell Technologies*), equipped with two Intel® Xeon® E5-2680 v2 (2.80 GHz) processors and 128 GB of RAM, using the dedicated MILabs.Rec software (*MILabs B.V.*, Version: 2.51.7).

The photopeak window was defined as 20%, thus a range of 126 to 154 keV and a corresponding photopeak of 140 keV were set. Based on the triple energy window (TEW) method, scatter correction was performed as described previously by Ogawa et al. [109].

For each collimator, reconstruction was performed by using the smallest possible voxel size of 0.1 mm for the XUHR-M and 0.2 mm for the GP-M and UHS-M. This was done to be able to achieve the highest feasible spatial resolution [110].

3.5.5. Elaboration of Suitable Reconstruction Parameters

As parameters noise, contrast, and contrast-to-noise ratio (CNR) were considered as a function of rod diameters. For calculation, the method first described by Walker et al. [111] was used and will be explained in paragraph **3.6.4**. For comparison, different

numbers of updates (=iterations*subsets) ranging from 128 to 640 were reconstructed and thus investigated. The first step was to assess how SROSEM performs compared to POSEM and MLEM. Therefore, two measurements of the 850.500 phantom using the UHS-M collimator, one representing a low-count and the other representing a high-count setting, were considered. Phantoms were filled with a tracer solution which had an activity concentration of 33.27 ± 3.39 MBq/ml. Study parameters were set to 10 bed positions (BP) with 10 s and 300 s time per bed position (TPB), respectively, resulting in about 2 min and 50 min scan time. Hereinafter, these measurements are referred to as "low-count level" and "high-count level", respectively, for ease of reference. Thereafter, the datasets were reconstructed by applying two different *NoU*, being 640 and 384. Respective reconstruction parameters were 1 *sb* with either 640 or 384 *it* for MLEM, 32 *sb* with 20 and 12 *it* for POSEM, and lastly 128 *sb* combined with 3 and 5 *it* for SROSEM. This analysis was complemented by an evaluation of varying *NoU* of SROSEM. Hence, a range of 128 up to 640 updates was analyzed looking at the same parameters mentioned above. The number of subsets was kept constant at 128 with a varying number of iterations from 1 to 5. All generated datasets were analyzed both quantitatively and visually concerning their image quality.

3.5.6. Data Processing

The acquired SPECT images were imported into the public domain software "A medical imaging Data Examiner" (AMIDE for Mac, version 1.0.5, Stanford, CA, USA) [112]. Firstly, a post-reconstruction 3D-Gaussian filter with adjusted kernel size was applied. For the calculation of the performance parameters explained below, different-sized cylindrical ROIs were placed.

Calculation and statistical analysis were performed using Microsoft® Excel® for Mac (Version 16.62, Microsoft365, Redmond, WA, USA).

3.6. Assessment of Performance Parameters

3.6.1. Sensitivity

The system's volume sensitivity for each collimator was assessed in accordance with the recommendations of the NEMA for preclinical PET scanners [97] as currently no dedicated preclinical SPECT protocol has been published. In this context, sensitivity

describes the registered photopeak counts per second (cps) R_i as a function of applied activity A_{cal} in [MBq] placed in the center of the FOV of the collimator to be assessed [49]:

$$Sensitivity = \frac{R_i}{A_{cal}} \tag{8}$$

Therefore, a point source consisting of ^{99m}Tc-pertechnetate was generated with an activity A_{cal} of 1.9 ± 0.1 MBq (mean ± standard deviation). The activity was measured in a dose calibrator (ISOMED 2010, Nuvia Instruments, Dresden, Germany). The volume of the solution was pipetted into Eppendorf® Safe-Lock Tubes® 1.5 ml (*Eppendorf AG*, Hamburg, Germany) made of polypropylene and was kept as low as possible (0.01 ml) to avoid attenuation that could influence the results. The corresponding vials were then placed in the center of the CFOV. The acquisition volume was set to 1 BP, equaling 7.9 ml, with a corresponding TPB of 5 min, equaling the total acquisition time. To reduce the statistical variability as much as possible, more than 100,000 counts per measurement were always detected.

3.6.2. Spatial Resolution

For the system's spatial resolution as a function of the collimator type selected, the three mini Derenzo phantoms, mentioned in section **3.3**, were used. A compilation of the phantoms' specifications can be found in **Table 2**. For better visualization **Figure 11a** shows CT images of the respective phantoms in an axial view. To reach the peak spatial resolution, the studies were carried out with high activity concentrations of 339.0 ± 39.1 MBq/ml. To ensure that all capillaries are completely filled, a small amount of conventional ink (Pelikan Ink 4001® Royal Blue, *Pelikan Holding AG*, Schindellegi, Switzerland) was added to the activity solution. Subsequently, the phantoms were placed in the center of the FOV. To cover the whole phantom, the acquisition volume was set to 9 BP for the 850.350 and 850.100 whereas for the 850.500 10 BP were needed. As the TPB was kept constant at 300 s, this results in a total acquisition time of 45 min and 50 min. Thereafter, reconstructed tomographic images were visually analyzed and the smallest still distinguishable rod size was interpreted as the maximum spatial resolution for the respective collimator. This technique had already been established by the system's predecessors [5, 6, 49, 88, 89].
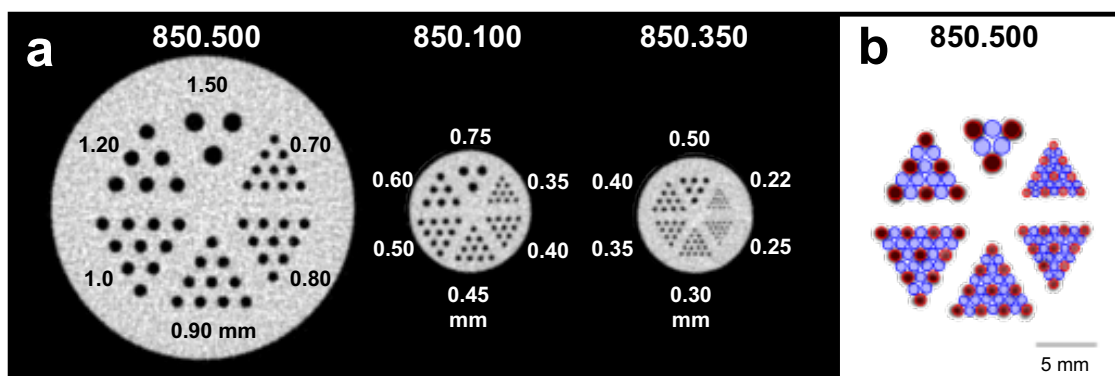
Figure 11: Specifications of used mini Derenzo hot-rod phantoms (**a**) and used template of multiple regions of interest for the contrast-to-noise ratio calculations (**b**).

The three used mini Derenzo phantoms are here shown as an axial view of tomographic CT images in (**a**). For assessment of the system's maximum spatial resolution all three phantoms were used and like this investigated rod sizes range from 1.50 down to 0.22 mm. The two phantoms 850.500 and 850.100 were also used for the contrast-to-noise ratio (CNR) calculations. Therefore, CT images were used to create a template consisting of blue and red regions of interest (ROI), placed on cold and hot regions, respectively. The size of each ROI was 6.0 mm in length and the diameter of the respective rod reduced by 10%. Thereafter, templates were placed on reconstructed SPECT images as exemplified in (**b**). This illustration shows the data for the 850.500 phantom acquired with the GP-M collimator over a scan time of 45 min with an activity concentration of 30 MBq/ml. For this image, the slice thickness was set to 6.0 mm. Adapted from *"Performance evaluation of fifth-generation ultra-high-resolution SPECT system with two stationary detectors and multi-pinhole imaging,"* by J. V. Hoffmann et al*.,* 2020, *EJNMMI Phys*, vol. 7, no. 1, pp. 1-15, Art no. 64 [31].

3.6.3. Uniformity

Image uniformity measurements were carried out for each of the three collimators. The evaluation of the system's uniformity is based on a phantom filled homogeneously with a ^{99m}Tc-pertechnetate solution with a comparable activity concentration of 322.8 ± 8.6 MBq/ml (see **3.3**). A cylindrical ROI, 7.5 mm in diameter and 6.0 mm in length, was drawn in the center of the phantom's filled chamber. Post-filtering with a three-dimensional Gaussian kernel identical to the assessed maximum spatial resolution was added. Thus, full width at half maximum (FWHM) was set to 0.35 mm for XUHR-M, 0.50 mm for GP-M, and 0.75 mm for UHS-M. The calculation was performed following the methodology defined by NEMA as follows [97]:

$$Uniformity\ (\%) = 100 \times \frac{Max\ count - Min\ count}{Max\ count + Min\ count} \tag{9}$$

3.6.4. Contrast-to-noise Ratio

Contrast-to-noise ratio was calculated in analogy to the methodology which was first described by Walker et al. [111]. Firstly, several studies with varied activity concentrations were performed on two mini Derenzo phantoms (850.100 and 850.500) to cover a wide range of rod diameters from 0.35 mm to 1.50 mm on the one hand. On the other hand, the different spectrum of activity concentrations is also intended to cover the low count ranges that occur in in vivo studies, particularly, when scan time and injection dose are limited, or uptake is low. All three collimators listed in **Table 1** were examined. Registered CT images of the respective hot-rod phantoms were then used to create a template for the CNR calculation. Therefore, cylindrical ROIs with a length of 6.0 mm and a 0.9 times capillary diameter were drawn on all rods for hot areas with high activity. For cold areas the sections in between the capillaries were used, dimensions of the ROIs were left identical. This is depicted in **Figure 11b** where red and blue circles represent hot and cold areas, respectively.

The calculation of contrast C_d and noise N_d was based on the following formulas as a function of the different-sized hot rod sections with diameter d:

$$C_d = \frac{\overline{R_d} - \overline{B_d}}{\overline{R_d}} \tag{10}$$

$$N_d = \frac{\sqrt{\sigma_{R_d}^2 + \sigma_{B_d}^2}}{\overline{ROIs_d}} \tag{11}$$

For evaluation of contrast, the mean value of all ROIs situated on hot areas $\overline{R_d}$ and cold areas $\overline{B_d}$ was determined. Image noise was calculated by using σ_{R_d}, and σ_{B_d} as standard deviations of hot and cold areas, whereas $\overline{ROIs_d}$ stands for the mean value of all ROIs for the respective diameter d to be investigated. To determine the CNR for each rod size, contrast and noise were then set in relation accordingly:

$$CNR_d = \frac{C_d}{N_d} \tag{12}$$

After reconstruction of the respective SPECT datasets, the images were then processed with a 3D-Gaussian filter to increase the image quality and positively enhance the CNR. The FWHM of the Gaussian kernel was defined to always match the corresponding rod size to be examined. For comparison of the three collimators XUHR-M, GP-M and UHS-M explained above acquisition time was set to 3 s, 30 s, and 300 s TPB. Measurements were conducted using either 32.8 ± 4.1 MBq/ml or 320.1 ± 6.5 MBq/ml as the activity concentration. To facilitate the comparison between the individual measurements, all activity concentrations were converted so that a measurement with a TPB of 300 s would have achieved a comparable count level. Hence, in **Figure 15** the descriptors ~0.3 MBq/ml, ~3 MBq/ml, ~30 MBq/ml, and ~300 MBq/ml were added. Total acquisition time resulted in 45 min since 9 BP were needed for the defined scan volume to cover the whole phantom.

Thereafter, image quality was assessed for the studies of all three collimators for rods ranging from 0.35 to 1.50 mm as a function of count levels. Furthermore, to better compare the image quality and rank the CNR values of the respective SPECT scans the images were evaluated visually considering the count- and collimator-dependent maximum spatial resolution.

3.7. Comparison Study

To give context to the data obtained, comparative measurements were carried out using the established predecessor U-SPECT$^+$ (*MILabs B.V.*) with three stationary detectors as explained in section **3.1.2**. For a more straightforward comparison, only the GP-M collimator with a 0.60 mm pinhole diameter was compared. The methodology of the performed scans was kept identical to that described for the two-detector system, using ^{99m}Tc-pertechnetate as the tracer.

The system's sensitivity was obtained with an activity concentration of 3.7 MBq in a point source placed in the CFOV. Scan volume was set to 1 BP with a total acquisition time of 5 min. For the evaluation of the collimator-dependent spatial resolution of the reconstructed tomographic images, the mini Derenzo phantom 850.100 was used (**Figure 11a, Table 2**). The applied activity concentration was 296.4 MBq/ml, scanning volume was covered by 12 BP with 300 s TPB resulting in a 60 min total acquisition time. Assessment of the uniformity was performed by using the cylindrical volume of the 850.100 phantom without the insert. Therefore, an activity concentration of 298.6 MBq/ml

with a filling volume of 1.5 ml was used. Acquisition parameters were set to 12 BP and 300 s TPB and thus a total scan time of 60 min. Lastly, CNR was also determined by using the 850.100 phantom with an activity concentration of 298.1 ± 1.6 MBq/ml and TPB of either 3 s, 30 s, or 300 s. Again, these acquisition parameters were converted to respective count levels of ~3 MBq/ml, ~30 MBq/ml and ~300 MBq/ml for a TPB of 300 s and a total acquisition time of 45 min. For these respective comparative measurements, the activity concentrations of all applied tracer solutions were determined using the dose calibrator CRC-127R (*CAPINTEC, Inc.*, Florham Park, NJ, USA).

4. Results

4.1. Elaboration of Suitable Reconstruction Parameters

4.1.1. Comparison of SROSEM, POSEM, and MLEM

Image quality analysis of the low-count level data showed that for all rod diameters examined from 0.70 to 1.50 mm, the highest CNR values were obtained for the new SROSEM algorithm with 384 *NoU*. This clear superiority could not be worked out for the high-count level. Although the CNR values deviate on average by only 4.16% from the respective best value, MLEM and POSEM are still slightly superior. For the high-count level SROSEM with 384 *NoU* provided the lowest image noise. Looking at both *NoU*s investigated, for all three reconstruction algorithms 384 showed better image quality than 640. The corresponding findings are shown in **Table 3** for the low-count level and in **Table 4** for the high-count level. **Figure 12** illustrates these data. Overall, SROSEM showed a slight advantage for the low-count level but at the same time slight weaknesses at the high-count level. On one hand, the data support that SROSEM is of comparable quality to the other two algorithms. On the other hand, the reconstruction time was significantly shorter, and hence the acquired data were reconstructed with SROSEM in this study [81, 113].

Reconstruction Algorithm (*NoU*)	Rod Diameter [mm]					
	0.70	**0.80**	**0.90**	**1.00**	**1.20**	**1.50**
MLEM (384)	0.311	0.454	0.514	0.536	0.696	0.899
POSEM (384)	0.303	0.449	0.506	0.526	0.689	0.869
SROSEM (384)	0.379	0.529	0.571	0.599	0.744	0.945
MLEM (640)	0.284	0.405	0.454	0.478	0.638	0.838
POSEM (640)	0.277	0.404	0.448	0.471	0.633	0.811
SROSEM (640)	0.335	0.458	0.487	0.529	0.675	0.856

Table 3: Contrast-to-noise ratio (CNR) values for the low-count comparison of reconstruction algorithms.
The values highlighted in red represent the peak CNR values for the respective rod diameter.

Reconstruction Algorithm (*NoU*)	Rod Diameter [mm]					
	0.70	0.80	0.90	1.00	1.20	1.50
MLEM (384)	1.046	1.241	1.302	1.150	1.351	1.797
POSEM (384)	1.050	1.234	1.300	1.146	1.355	1.803
SROSEM (384)	0.961	1.195	1.243	1.116	1.310	1.767
MLEM (640)	0.971	1.146	1.218	1.105	1.336	1.759
POSEM (640)	0.974	1.140	1.217	1.102	1.339	1.764
SROSEM (640)	0.882	1.086	1.146	1.055	1.288	1.705

Table 4: Contrast-to-noise ratio (CNR) values for the high-count comparison of reconstruction algorithms.

The values highlighted in red represent the peak CNR values for the respective rod diameter.
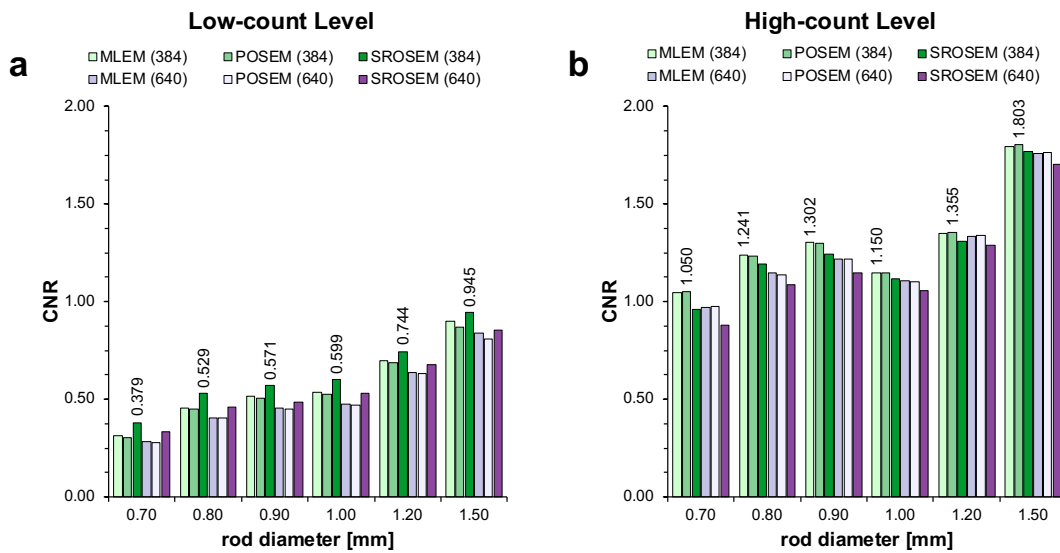
Figure 12: Comparison of MLEM, POSEM and SROSEM for (**a**) low- and (**b**) high-count conditions.

The charts are illustrating the data collected for the 850.500 phantom in combination with the UHS-M collimator. The highest contrast-to-noise ratio value obtained for each rod diameter was indicated above the corresponding bar. The studies reconstructed with the same number of updates were grouped side by side for each rod diameter: 384 on the left (shades of green) and 640 on the right (shades of purple).

4.1.2. Evaluation of Reconstruction Parameters for SROSEM

The subsequent comparison of the varying *NoU* using SROSEM with 1 to 5 *it* is compiled in **Figure 13** and respective data is listed in **Table 5**. The evaluation could demonstrate the following. With respect to the rods in the submillimeter range (0.70; 0.80; 0.90 mm), increasing the number of iterations above 3 showed a deterioration of the CNR. In contrast, the two largest rods of 1.20 and 1.50 mm do benefit from a higher number of updates and thus the respective peak CNR was reached at 4 *it*. The mean noise increases consistently with rising NoU, while the mean contrast is superior at 3 *it*. To combine a low noise level with high contrast for each rod size applicable to a wide range of counts, 3 *it* with 128 *sb* seems to be favorable.

SROSEM (128 *sb*)	Rod Diameter [mm]					
	0.70	0.80	0.90	1.00	1.20	1.50
1 *it*	1.008	1.318	1.373	1.276	1.128	1.485
2 *it*	1.031	1.259	1.298	1.202	1.225	1.671
3 *it*	0.961	1.195	1.243	1.116	1.310	1.767
4 *it*	0.859	1.084	1.169	1.016	1.342	1.766
5 *it*	0.633	0.859	0.992	0.799	1.224	1.579

Table 5: Contrast-to-noise ratio (CNR) values for the evaluated number of updates of SROSEM. The values highlighted in red represent the peak CNR values for the respective rod diameter.
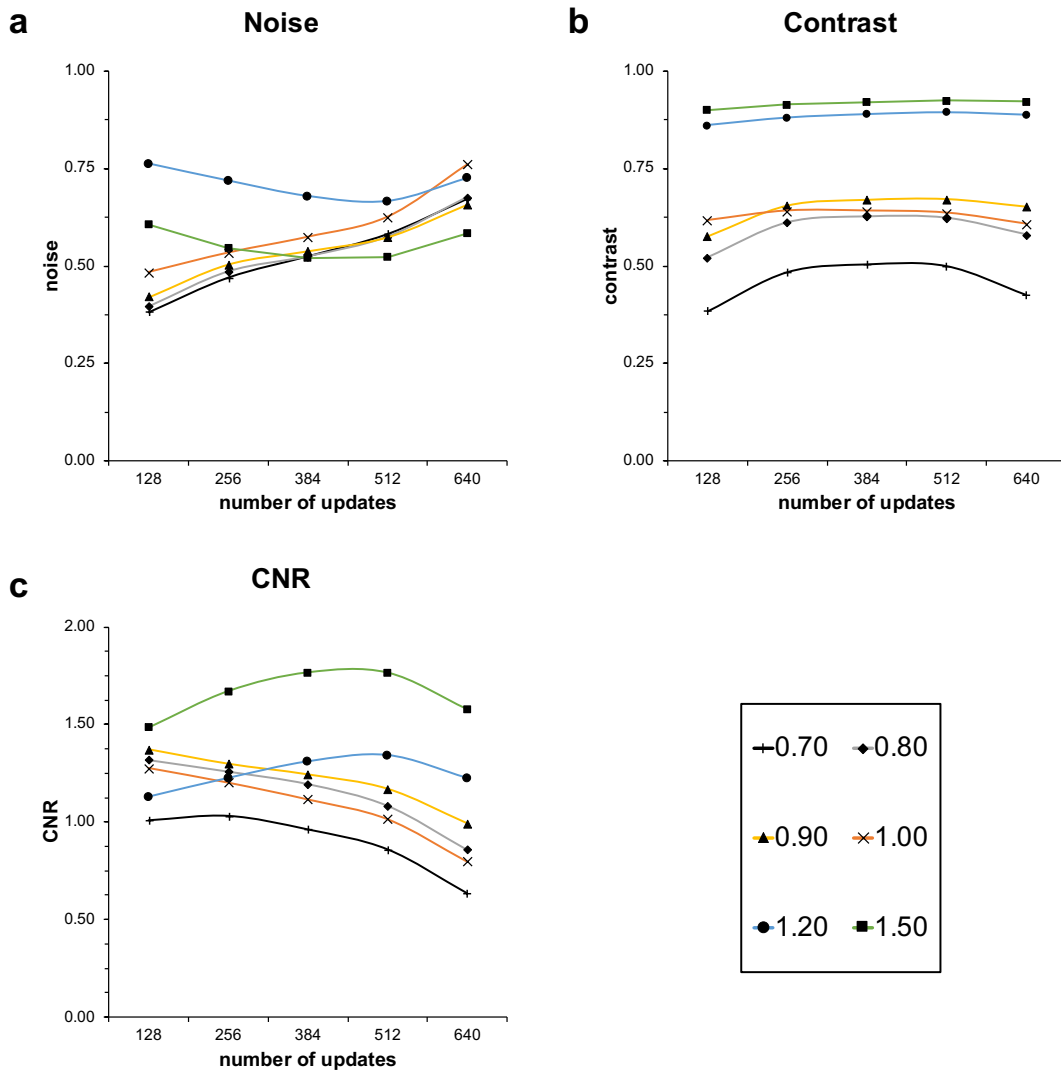
Figure 13: Noise (**a**), contrast (**b**), and contrast-to-noise ratio (**c**) of the different rod diameters [mm] as a function of the number of updates of SROSEM.

The data shown are calculated based on images obtained using the 850.500 phantom and the UHS-M collimator. The number of subsets was kept constant at 128 and iterations varied from 1 to 5. The activity concentration applied was 33.27 ± 3.39 MBq/ml and the acquisition time was 50 min.

4.2. Sensitivity

The two-headed U-SPECT[5] E-Class achieved a peak sensitivity of 239 cps/MBq (0.024%) for the XUHR-M collimator, 892 cps/MBq (0.089%) for the GP-M collimator and for the UHS-M collimator it was 2257 cps/MBq (0.226%).

With the established three-detector U-SPECT[+], a maximum sensitivity of 1775 cps/MBq (0.178%) was achieved. The direct comparison of the values obtained with the GP-M collimator shows that the three-detector system achieved more than double the peak sensitivity of the updated version using only two detectors (cf. **Table 6**).

| Collimator type | U-SPECT[5] E-Class | | | U-SPECT[+] |
	XUHR-M	GP-M	UHS-M	GP-M
Peak sensitivity [cps/MBq]	239	892	2257	1775
Spatial resolution [mm]	0.35	0.50	0.75	0.50
Uniformity [%]	41.3	31.2	23.0	16.3

Table 6: Compilation of the examined values for both U-SPECT scanners.

4.3. Spatial Resolution

The tomographic images of the mini Derenzo phantoms were visually evaluated and resulted in a maximum spatial resolution for the two-detector system of 0.35 mm using the XUHR-M. For the GP-M collimator rods with a diameter of 0.50 mm could be discriminated, whereas for images acquired with the UHS-M collimator a peak spatial resolution of 0.75 mm was achieved. Considering the comparative data registered with the three-detector setup, it was neither possible to distinguish capillaries with a diameter smaller than 0.50 mm (cf. **Table 6**). The corresponding SPECT images, with the use of which this analysis was carried out, are compiled in **Figure 14a**.
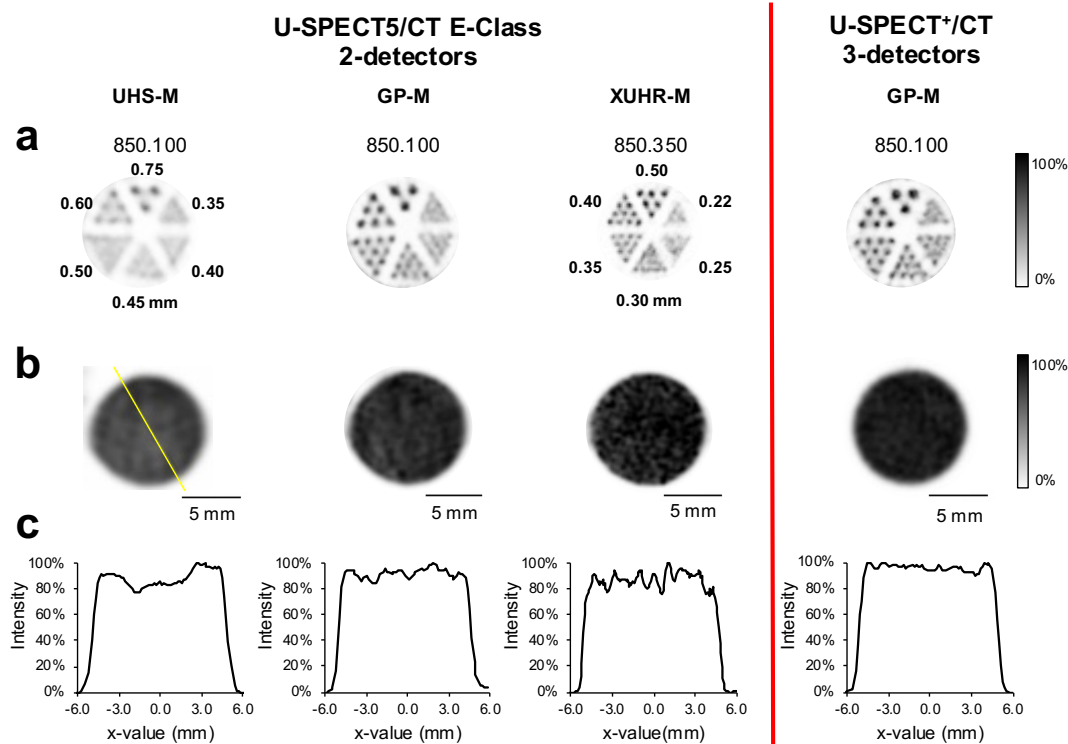
Figure 14: Compiled results for (**a**) tomographic spatial resolution in hot-rod phantoms and (**b**) uniformity of a cylindrical volume with corresponding line profile (**c**).

The first three columns show the studies for the UHS-M, GP-M, and XUHR-M mouse collimators examined with the U-SPECT[5]/CT E-Class two-detector device. For comparison, the last column shows data obtained for the same GP-M collimator using the three-headed predecessor U-SPECT[+]/CT. The corresponding source for which the line profiles are plotted in (**c**) is shown in yellow in the first phantom image to the left of (**b**). The slice thickness of the depicted SPECT images was set to the smallest available at 0.2 mm for UHS-M and GP-M or 0.1 mm for XUHR-M, respectively. Adapted from *"Performance evaluation of fifth-generation ultra-high-resolution SPECT system with two stationary detectors and multi-pinhole imaging,"* by J. V. Hoffmann et al., 2020, *EJNMMI Phys*, vol. 7, no. 1, pp. 1-15, Art no. 64 [31].

4.4. Uniformity

Evaluation of the uniformity studies for all three examined collimators following the specifications of the NEMA protocol yielded 41.3% for XUHR-M, 31.2% for GP-M, and 23.0% for UHS-M. The collimator GP-M in the three-detector scanner was able to achieve a uniformity of 16.3%, which means that it outperformed all the data obtained for the two-detector system. For better illustration, respective images and line profiles are composed in **Figure 14b, c**.

4.5. Contrast-to-noise Ratio

Results of the image quality studies for the three respective collimators are summarized in **Figure 15** as CNR values for four various count ranges as a function of the rod size of the analyzed mini Derenzo phantoms. For better visualization, reconstructed images are compiled in **Figure 16** for the 850.500 and in **Figure 17** for the 850.100 phantom. **Figure 19** compiles the collimators' achieved spatial resolution for four different count levels.

4.5.1. UHS-M

As the UHS-M collimator was designed for low-activity conditions it showed its potential in the studies with an activity concentration of 0.3 MBq/ml for higher rod diameters of 0.80 to 1.20 mm. Here the CNR values range from 0.37 to 1.55. Highest CNR was achieved for the rod size of 1.50 mm counting 1.78. Nevertheless, the peak CNR for this rod size was reached by the GP-M collimator with 2.09. Considering the data obtained with 3 MBq/ml as activity concentration UHS-M prevailed over the two other collimators for rods sized 1.2 and 1.5 mm. Here, CNR values were 1.96 and 2.29, respectively. An increase in the activity concentration to 30 and 300 MBq/ml led to a further gain in CNR values. Looking at rods representing the maximum spatial resolution of 0.75 mm, peak CNR was calculated for the 30 MBq/ml activity concentration and amounts to 1.94, which represents a usable image quality as seen in **Figure 17**. The study with the highest activity concentration of 300 MBq/ml showed no advantage with respect to image quality. In fact, a decrease in CNR values was found for the 0.75 mm rod diameter, which is 1.87 compared to the 1.94 found at 30 MBq/ml. For the SPECT scans using the smaller 850.100 CNR values for rods below 0.75 mm were not meaningful, since this is the maximum spatial resolution of the UHS-M collimator.

4.5.2. GP-M

The contrast-to-noise ratio of the SPECT scans using the GP-M collimator was superior especially for the mid-range activity concentrations of 3 MBq/ml and 30 MBq/ml. Using 3 MBq/ml, the GP-M prevailed for rod diameters of 1.0 to 0.70 for the 850.500 and 0.75 as well as 0.60 mm for the 850.100 phantom. Diameters of 1.5 and 0.90 to 0.70 mm with CNR values ranging from 2.24 to 0.80 were best compared to the two other collimators for 30 MBq/ml. Reconstructed images acquired with an activity concentration of 0.3 MBq/ml show superior CNR values for 1.5, 0.75, and 0.70 mm. The highest activity

concentration applied was able to increase the CNR values by more than 0.6 times for the section of rods with a 0.5 mm diameter, which corresponds to the maximum spatial resolution. For bigger rods, there was only a slight benefit with an increase of 23% and 3% for rod diameters of 0.60 and 0.75 mm. The Peak CNR value was achieved for the 1.5 mm rod and was 2.52 with an activity concentration of 30 MBq/ml. The highest CNR for the rods representing the maximum spatial resolution of 0.50 mm was 1.42 for the 300 MBq/ml activity concentration.

4.5.3. XUHR-M

For the lowest activity concentration of 0.3 MBq/ml, 0.75-millimeter-sized rods were visually not discriminable but slightly indicated and the corresponding CNR value was 0.28. However, at the same time, minor image quality was achieved, especially if compared to the images using UHS-M or GP-M with values of 0.56 and 0.82, respectively. For the three remaining activity concentrations, CNR values for rods sized 0.35 to 0.50 mm were superior by using the XUHR-M. By visually assessing the maximum spatial resolution, for the 3 MBq/ml measurements, only rods sized 0.60 mm or higher could be discriminated. Corresponding CNR values range from 0.90 for 0.60 mm to 2.20 for 1.50 mm. Activity concentration of 30 MBq/ml results in superior CNR values for rod sizes from 0.35 to 0.75 mm ranging from 0.18 up to 2.23. Applying 30 MBq/ml led to discriminable rod sizes up to 0.40 mm with a CNR value of 0.38. With the highest used activity concentration of 300 MBq/ml, the system was capable to resolve even rods with a diameter of 0.35 mm with a respective CNR value of 0.22. For this activity concentration, the XUHR-M reaches the highest CNR compared to the other collimators for the rod range of 0.35 mm with 0.22 to 0.75 mm with 2.57. The maximum increase was achieved for the 0.40-millimeter capillaries and was 220%.
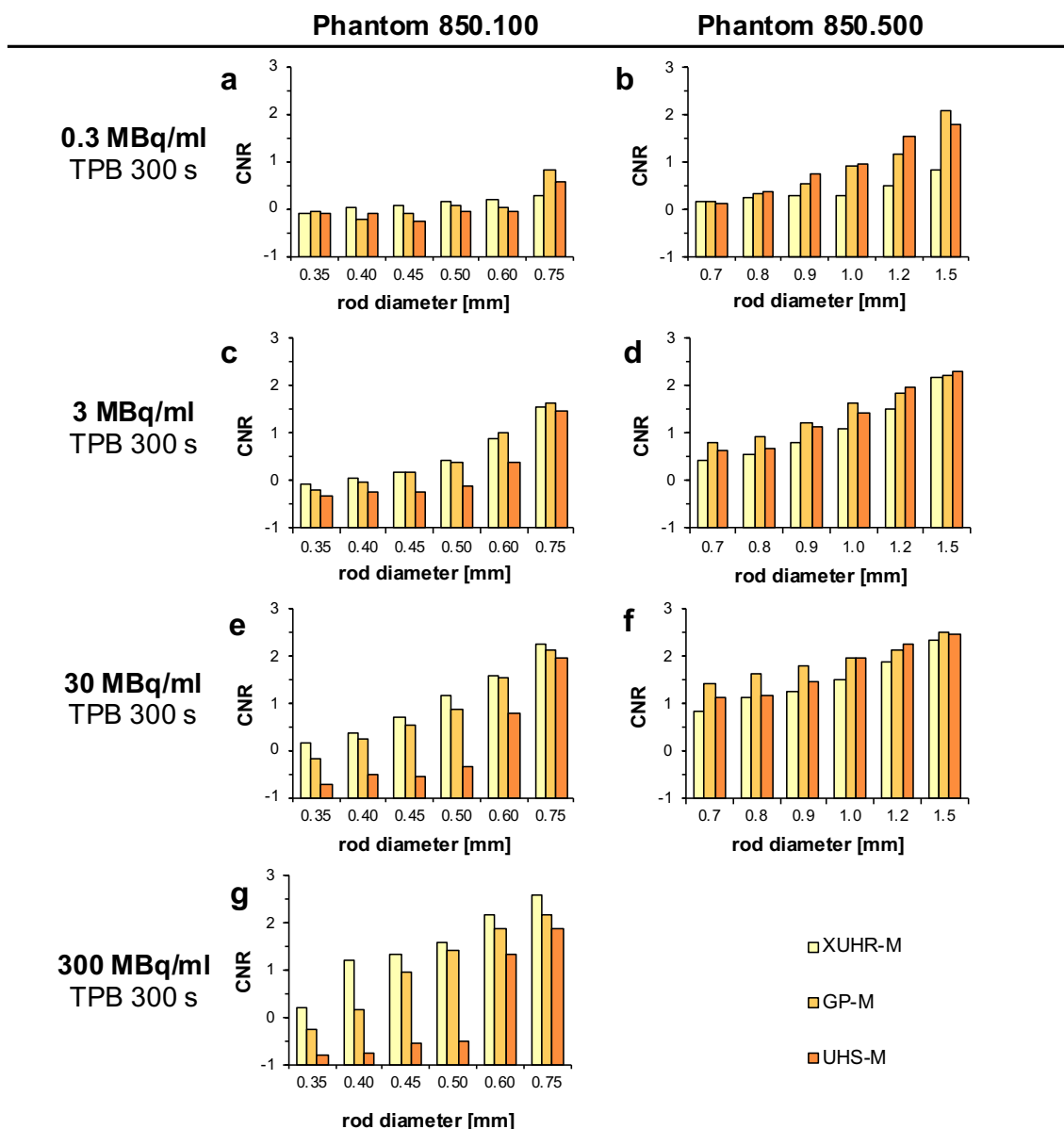
Figure 15: Contrast-to-noise ratio as a function of investigated rod diameters.

Contrast-to-noise ratio (CNR) values are plotted against the rod diameters of the mini Derenzo phantoms 850.100 and 850.500 for the four activity concentrations examined. For each rod size, the CNR values were Gaussian post-filtered with full width at half maximum (FWHM) equaling the respective rod diameter. The bar graphs represent the image quality of the three collimators XUHR-M, GP-M, and UHS-M for the U-SPECT[5]/CT E-Class. Acquisition parameters were 300 s as time per bed position (TPB) and 9 bed positions (BP) for the 850.100 or 10 BP for the 850.500 resulting in a total scan time of 45 min and 50 min, respectively. Adapted from *"Performance evaluation of fifth-generation ultra-high-resolution SPECT system with two stationary detectors and multi-pinhole imaging,"* by J. V. Hoffmann et al.*, 2020, EJNMMI Phys*, vol. 7, no. 1, pp. 1-15, Art no. 64 [31].
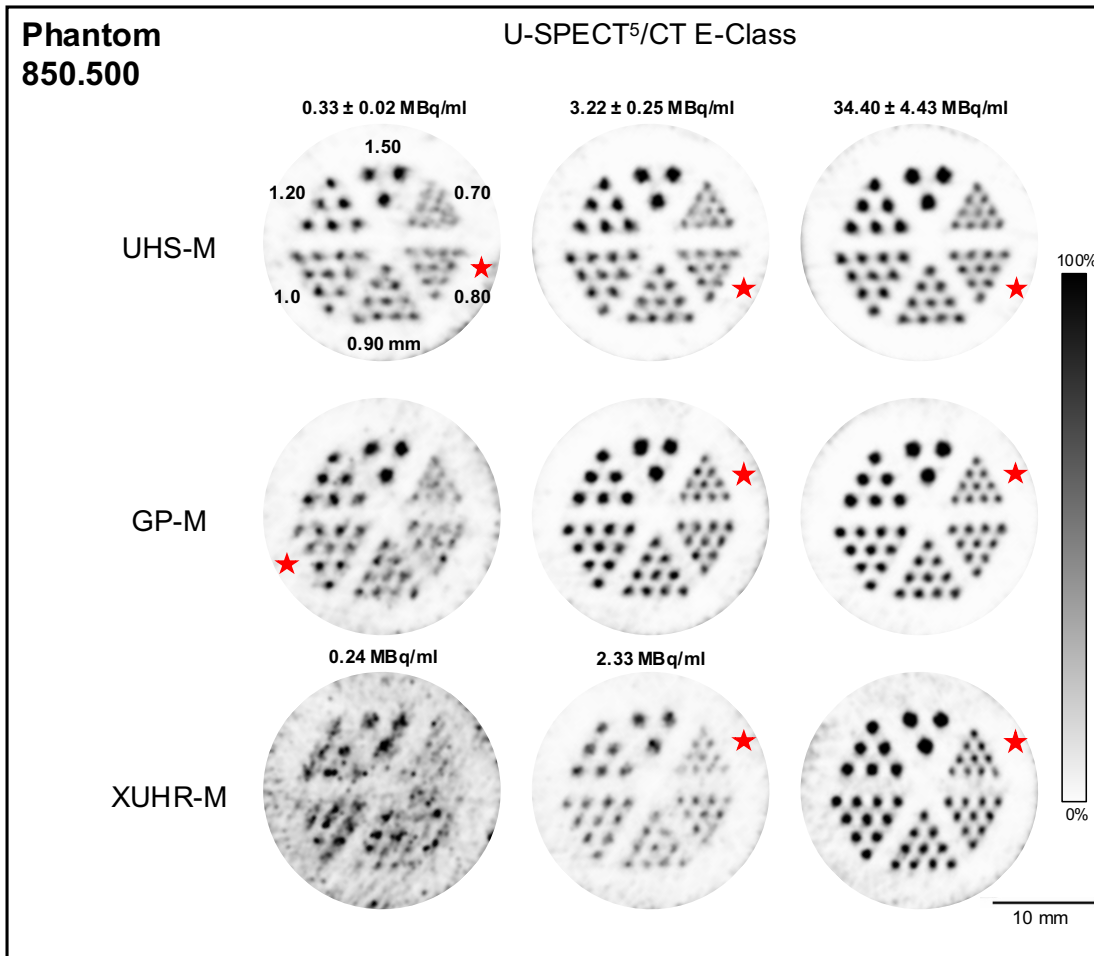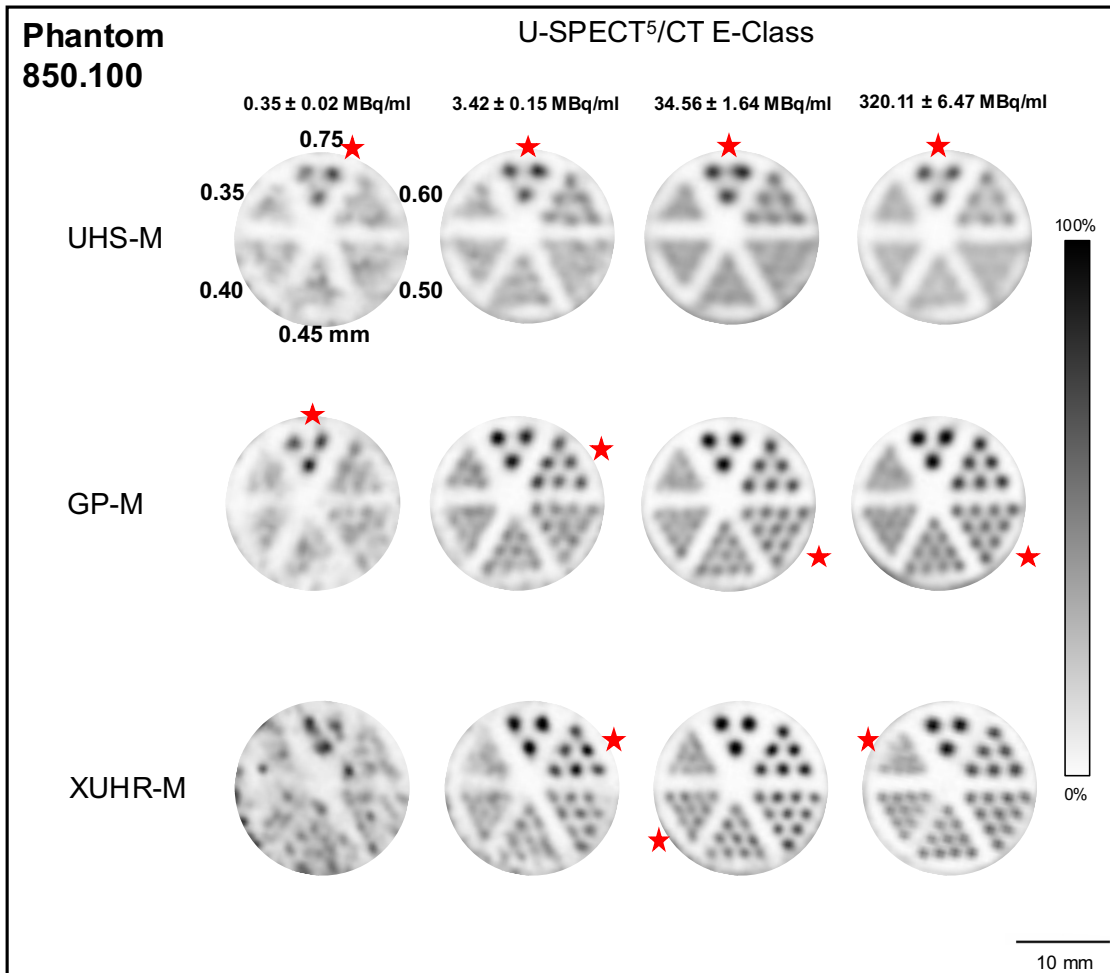
Figure 16: Examined SPECT images for the contrast-to-noise ratio analysis using the 850.500 phantom.

The figure shows a compilation of SPECT images from the 850.500 mini Derenzo phantom for the three mouse collimators examined at changing activity concentrations (mean ± standard deviation). The tracer applied was ^{99m}Tc-pertechnetate and the acquisition parameters were defined as 300 s time per bed position (TPB), and 10 bed positions (BP). The slice thickness of the images was set to 6.0 mm and a Gaussian post-filter with a full width at half maximum (FWHM) of 0.35 mm was applied. The red stars mark the smallest rod section which was still rated as resolvable. Adapted from "*Performance evaluation of fifth-generation ultra-high-resolution SPECT system with two stationary detectors and multi-pinhole imaging,*" by J. V. Hoffmann et al., 2020, *EJNMMI Phys*, vol. 7, no. 1, pp. 1-15, Art no. 64 [31].

Figure 17: Examined SPECT images for the contrast-to-noise ratio analysis using the 850.100 phantom.

The figure shows a compilation of SPECT images from the 850.100 mini Derenzo phantom for the three mouse collimators examined at changing activity concentrations (mean ± standard deviation). The tracer applied was ^{99m}Tc-pertechnetate and the acquisition parameters were defined as 300 s time per bed position (TPB), and 9 bed positions (BP). The slice thickness of the images was set to 6.0 mm and a Gaussian post-filter with a full width at half maximum (FWHM) of 0.35 mm was applied. The red stars mark the smallest rod section which was still rated as resolvable. Adapted from *"Performance evaluation of fifth-generation ultra-high-resolution SPECT system with two stationary detectors and multi-pinhole imaging,"* by J. V. Hoffmann et al., 2020, *EJNMMI Phys*, vol. 7, no. 1, pp. 1-15, Art no. 64 [31].

4.5.4. GP-M: Comparison of U-SPECT^5 E-Class and U-SPECT$^+$

The maximum achievable spatial resolution for both the three- and two-detector setup was 0.50 mm, which was only reached for the scans with 30 and 300 MBq/ml applied. Here, CNR values were 0.92 and 1.06 for the three-detector configuration whereas 0.87 and 1.42 for the two-detector setup. For the activity concentration of 3 MBq/ml rods with a 0.60 mm were discriminable with a respective CNR value of 0.78 (U-SPECT$^+$) and 1.02 (U-SPECT^5 E-Class). Peak CNR achieved with the three-detector system was 2.27 for 0.75 mm with 300 MBq/ml, whereas the two-detector setup could only achieve 2.19 with the same study parameters. Looking at the values, no system configuration is clearly superior to the other, as the CNR values differ by an average of 3.6%. To visualize comparable image quality, the results are summarized in **Figure 18**.

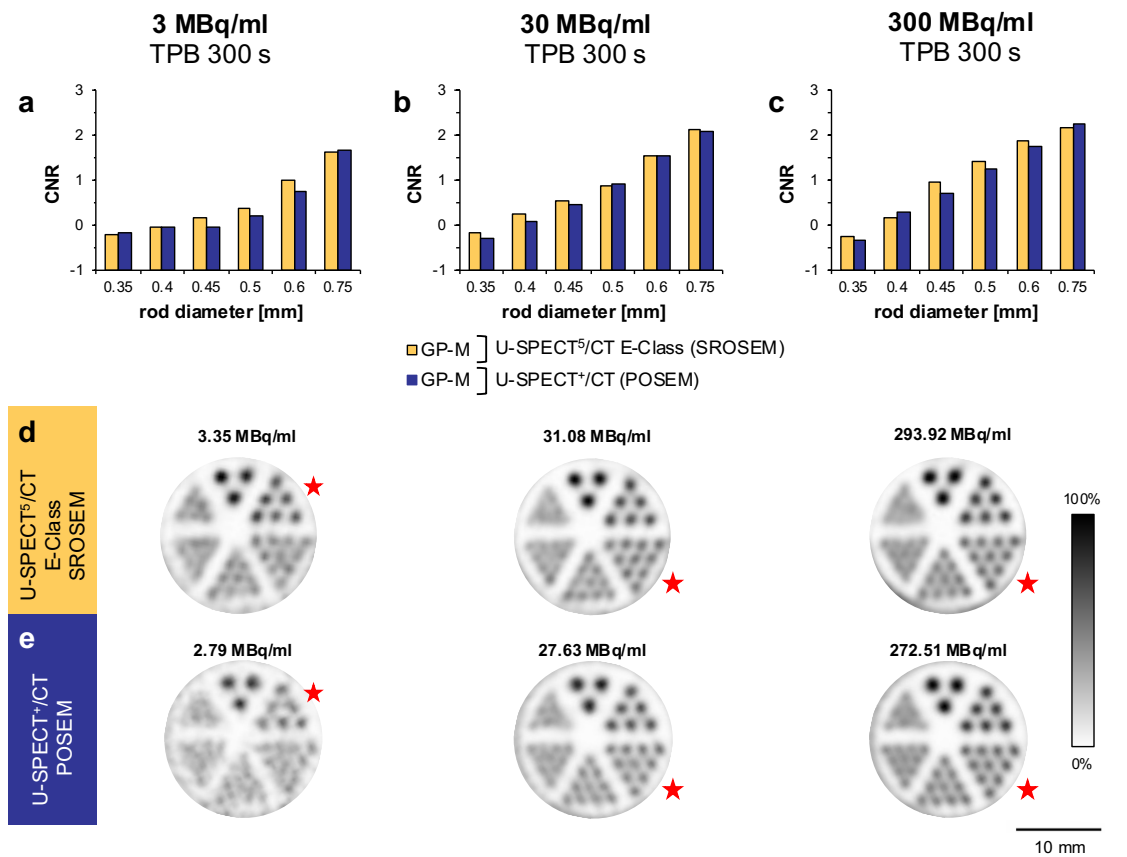**Figure 18:** Contrast-to-noise ratio of the GP-M collimator for both the U-SPECT[5]/CT E-Class and U-SPECT[+]/CT.

This is an illustration of the comparison of the U-SPECT[5]/CT E-Class (orange) and U-SPECT[+]/CT (blue) systems with the GP-M collimator. Bar graphs (**a**), (**b**), and (**c**) show the assessed contrast-to-noise ratio (CNR) values for studies at 3; 30; and 300 MBq/ml as a function of rod diameters in [mm] using the 850.100 mini Derenzo phantom. A Gaussian post-filter with full width at half maximum (FWHM) = rod diameter was applied for each rod section. To better illustrate these values, the corresponding SPECT images are compiled in (**d**) for the U-SPECT[5]/CT E-Class and (**e**) for the U-SPECT[+]/CT. For acquisition, time per bed position (TPB) was set to 300 s with 9 bed positions (BP) for the U-SPECT[5]/CT E-Class and 12 BP for the U-SPECT[+]/CT. The slice thickness of the sample images is 6.0 mm and a Gaussian post-filter of 0.35 mm as FWHM was applied. The red stars mark the smallest rod size that was found to be distinguishable. Adapted from *"Performance evaluation of fifth-generation ultra-high-resolution SPECT system with two stationary detectors and multi-pinhole imaging,"* by J. V. Hoffmann et al., 2020, *EJNMMI Phys*, vol. 7, no. 1, pp. 1-15, Art no. 64 [31].

5. Discussion

In this study, the capabilities of a recently launched dedicated small-animal micro-SPECT device with two large stationary detectors combined with multi-pinhole collimation were investigated. In addition, a comparison with an established micro-SPECT scanner using a conventional three-detector setup was performed to benchmark the assessed performance parameters. Considering the one-third reduction in detection area, sensitivity, and image quality in particular in low-count scenarios were expected to be challenging. But at the same time, these are indispensable for in vivo studies since an infinite increase in injection dose and scan time under anesthesia is not allowed by applicable regulations for animal experimentation and is also incompatible with animal health. With this challenge in mind, the goal of this work was to create a tool to better estimate performance as a function of count level in future in vivo studies. As already highlighted in my introduction there are many preclinical animal models well established. In consequence, translation from in vivo studies with small rodents to humans is easy for the development of new tracers. With the improved integration of CT data, it is now possible to really benefit from the additional information deriving from the CT unit. Hence, the clinical value and diagnosability of obtained images are improved and an increase in the number of clinical applications is expected [21-27]. Another aspect that was a major driver for conducting this study was, that usually performance evaluations are mainly focused on achieving the maximum in all parameters. Thus, it has been common practice to apply high activity concentrations without considering that these results are not quite transferable to in vivo studies with small animals (van der Have et al.: 600 MBq/ml [49], Deleye et al.: 500 MBq/ml [93], Matsunari et al.: 370 MBq/ml [104], Ivashchenko et al.: 1200 MBq/ml [5]). Therefore, in this work, the investigated count levels were extended to activity concentrations from about 0.3 MBq/ml up to 300 MBq/ml.

Due to the need for collimation, the evaluation of volume sensitivity is the most challenging part of small-animal SPECT imaging. Hence, the examined volume sensitivity for each collimator in the CFOV clearly showed that the UHS-M collimator achieved the highest overall value of 2054 cps/MBq (0.205%). As expected, with 847 cps/MBq (0.085%) for the GP-M and 237 cps/MBq (0.024%) for the XUHR-M, these two collimators could not keep up. Considering the larger detection area of the three-detector configuration, it is surprising that the sensitivity of 1710 cps/MBq (0.171%) for the three-detector configuration with the same GP-M collimator is twice as high as the sensitivity obtained with the two-detector arrangement. However, when these values are compared

with data from previously published performance evaluations, it is clear that despite the reduced size of the detection area, the system outperforms other available preclinical SPECT scanners. Those only achieved sensitivities between 35.3 and 751.0 cps/MBq [93, 102, 104, 114]. With respect to the precursor model, U-SPECT-II revealed the potential of combining large stationary detectors with multi-pinhole collimation. Published data showed that this system with a multi-pinhole collimator with a 1-millimeter pinhole diameter could achieve a peak sensitivity of up to 3984 cps/MBq [93]. Using a special collimator in the U-SPECT[+], Ivashchenko et al. even found out that sensitivities of 13080 cps/MBq were feasible. However, this happened at the expense of spatial resolution [89]. These findings underline the impact of the decreased size of the detection area, as it is indispensable for the peak registered number of counts [115].

Likewise, in terms of uniformity, the U-SPECT[5]/CT E-Class achieves the best values using the UHS-M collimator. While the integral uniformity with this collimator is 23%, the GP-M and XUHR-M are only able to achieve 31.2 and 41.3%, respectively. Regarding this parameter, it was also possible to determine a certain advantage of the three-detector system, since here the uniformity with the GP-M was 16.3%. It can be assumed that in consideration of the missing lower detector and restricted sensitivity the limited image uniformity is caused by the fact that the photons directed downward are not included in the image calculation [116].

As the high spatial resolution is crucial when imaging small rodents, this parameter defines the usability of such a system for preclinical research. Overall, each investigated collimator was able to achieve submillimeter resolution. As expected, peak spatial resolution was determined using the XUHR-M collimator and is 0.35 mm, with 0.50 and 0.75 mm for the GP-M and UHS-M collimator the system consistently proves state-of-the-art spatial resolution when compared to previously published data [5, 49, 93, 95, 102]. Considering the study with the predecessor model U-SPECT[+], no higher spatial resolution with the GP-M collimator with pinholes 0.60 mm in diameter could be obtained, so it stays at 0.50 mm. Data from literature suggest that this collimator can also differentiate rods with a diameter of up to 0.35 mm [5]. However, this could not be confirmed with the experimental parameters of this study. This may be attributed to the applied study protocol of Ivashchenko et al. with an activity concentration of 1200 MBq/ml and an acquisition time of more than 2 h compared to 300 MBq/ml and just below 1 h for the measurements in this work [5]. Recently published data of a U-SPECT/CT

demonstrates that even a spatial resolution of 0.15 mm can be achievable by scanning hot-rod phantoms with a dedicated autoradiography collimator for tissue samples [117]. Nevertheless, based on these data, it can be expected that the two-detector system, especially with the XUHR-M collimator, can resolve even smaller rods. Referring to its pinhole size of 0.25 mm a respective maximum resolution of 0.25 mm might be realized [5].

Yet, it must be emphasized that the relevance of these imaging protocols for preclinical in vivo studies is doubtful. Conclusively, the two-headed micro-SPECT scanner was on par with the three-headed configuration in terms of tomographic spatial resolution in a head-to-head comparison. This can most likely be attributed to the collimator design and pinhole diameter. However, also for the applied improved reconstruction algorithm, it could be shown that this algorithm positively affects the spatial resolution [81]. Even though the tomographic spatial resolution is often evaluated axially and transaxially by using a line source (especially when looking at SPECT scanners) the use of iterative reconstruction algorithms utilizing mini Derenzo phantoms instead is common practice. There are several reasons for following this approach. Firstly, line source spatial resolution may be reproducible and hence be a good benchmark for the intercomparison of different systems. But a translation to animal scans and tomographic images is not easily possible and so these tests do not give a reasonable indication of the resolution that can be expected in practice. Furthermore, especially when iterative reconstruction algorithms, like MLEM or OSEM, are applied, it has been shown that due to increased sensitivity by multiplexing may lead to an overestimation of the system's spatial resolution as it is especially beneficial for singular objects with clearly limited accumulations of radioactivity. This advantage is relativized with more complex geometries like the mini Derenzo phantoms used here, due to increased overlapping of the registered projections [118, 119]. Deleye et al. [93] were able to demonstrate this overestimation in their work by assessing the spatial resolution achieved with the line source as well as with mini Derenzo phantoms. Thus, the X-SPECT of *GE Healthcare*, relying on multiplexing, reached a maximum spatial resolution of 0.49 mm with a line source, but only 0.6 mm in a hot-rod phantom, whereas *MILabs'* predecessor model U-SPECT-II provided 0.38 mm in the line source measurement and rod sizes of 0.4 mm could also be distinguished. Consequently, the assessment of spatial resolution with mini Derenzo phantoms better reflects the actual resolution of the respective system in reconstructed images and allows easier inter-system comparison. Lastly, the published

maximum spatial resolutions of *MILabs*' precursor U-SPECT scanners are also based on this methodology, so a direct comparison is very easily made [5, 49, 87]. However, a disadvantage of this method is the assumption that the same spatial resolution is achieved in the entire slice, which may not necessarily correspond to reality in the case of inadequate calibration.

With respect to the data collected from the mini Derenzo phantoms filled with different activity concentrations, four major observations can be made when considering the maximum distinguishable rod sizes as markers for the expected count-dependent spatial resolution. Firstly, for the lowest applied activity concentration of just around 0.3 MBq/ml submillimeter spatial resolution was achievable for both the UHS-M and GP-M collimator as rods as small as 0.75 mm in diameter were discriminable. Secondly, to take advantage of the XUHR-M collimator, at least 3.0 MBq/ml was required to reach a sufficiently high-count level, otherwise, the background noise is simply too high. However, to fully exploit the potential of this collimator, activity concentrations of at least 30 MBq/ml are required. Only then it is superior to the GP-M collimator in particular in terms of spatial resolution as rods with a diameter of up to 0.40 mm can be differentiated compared to 0.50 mm for the GP-M. Thirdly, according to the manufacturer's recommendations and as the name GP-M suggests, this collimator was able to handle the widest range of counts and to achieve the maximum spatial resolution of 0.50 mm already at 30 MBq/ml. Since the XUHR-M with 0.40 mm shows only a slight improvement in resolution at the same count level and there is no difference in resolution at 0.3 MBq/ml compared to the UHS-M, the GP-M convinced as a true all-rounder. Lastly, it must be admitted that although the XUHR-M shows the potential of the system in terms of maximum spatial resolution with 0.35-millimeter rods being discriminated, such high-count levels are hardly reached in in vivo whole-body scans. Therefore, this collimator is reserved for either focused scans of organs or post-mortem studies. **Figure 19** illustrates the count-dependent spatial resolution of all collimators investigated.
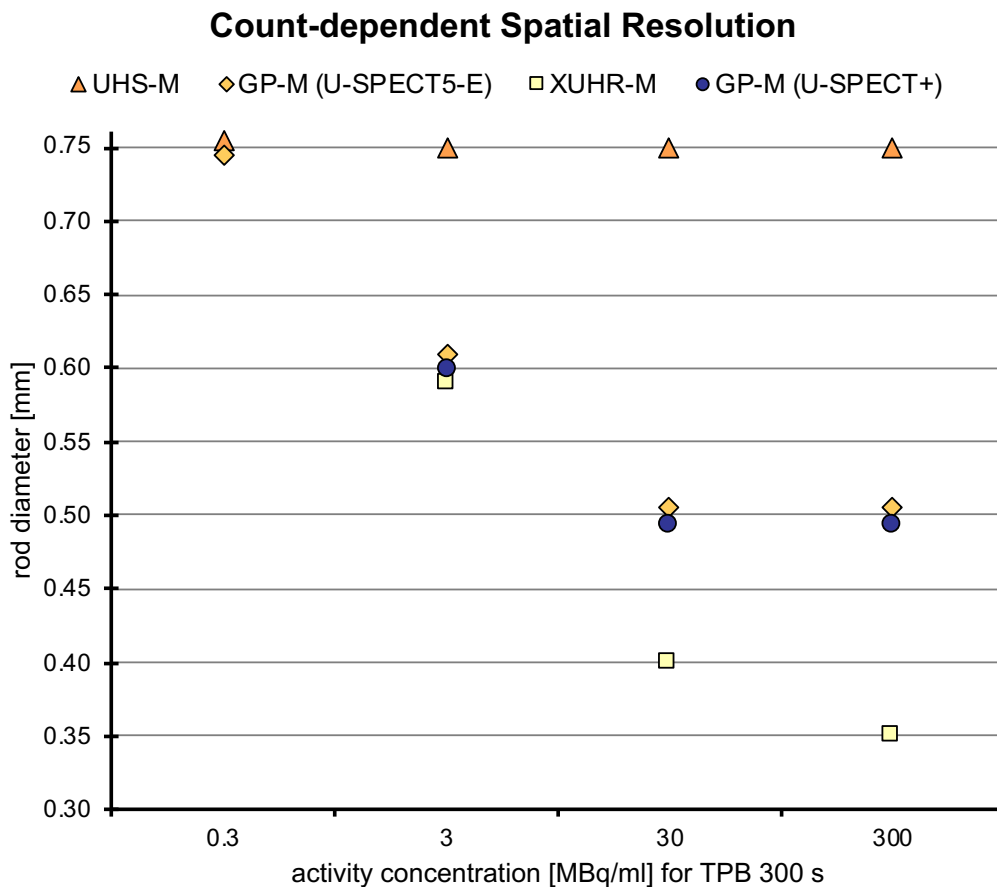
Count-dependent Spatial Resolution

△ UHS-M   ◇ GP-M (U-SPECT5-E)   ☐ XUHR-M   ● GP-M (U-SPECT+)

Figure 19: Count-dependent spatial resolution of the investigated collimators.

The maximum spatial resolution in [mm] achieved for all three collimators studied is shown as a function of the four different activity concentrations in [MBq/ml]. No rod was distinguishable for the XUHR-M in the study with 0.3 MBq/ml. Comparative values obtained in the study with the GP-M in the U-SPECT[+] are added for 3, 30, and 300 MBq/ml, respectively.

Based on the applied CNR analysis method as an indicator for image quality, the key findings can be summarized as follows. The UHS-M collimator is superior for the low-count scenario of 0.3 MBq/ml. In combination with the assessed point source sensitivity, this collimator turned out to be a good choice for overview measurements and especially at small activity doses applied. Furthermore, even at these low levels of activity concentration, the reconstructed images are visually very low in background noise. Despite this, the measurements with 3.0 MBq/ml as activity concentration result in higher CNR values. However, for studies with 3.0 MBq/ml or even higher activity concentrations using the GP-M collimator, superior CNR values have been obtained for most rod diameters and visually there is no noticeable difference in terms of image quality. Consequently, and taking into consideration its maximum spatial resolution of 0.50 mm,

it is proposed to switch to the GP-M collimator at these activity concentrations. Overall, the GP-M collimator performed better at the activity concentration of 3.0 MBq/ml, but nearly as well as the XUHR-M with 30 MBq/ml. When examining the data collected with the XUHR-M, it is noticeable that in the range of 0.60 to 0.35 mm, almost all CNR values were higher than those of the two alternatives, provided that the rods could also be visually distinguished. Only at the activity concentration of 3 MBq/ml, the CNR value for the 0.6-millimeter rods with the GP-M is 14.5% larger at 1.02 compared to 0.89. At 0.3 MBq/ml the CNR values for the low-count setting are close to zero or even negative. This combined with the visual assessment confirms that activity concentrations of at least about 3.0 MBq/ml are required for useful image quality, although activity concentrations of 300 MBq/ml or higher represent the real potential. Nevertheless, the eventual drawbacks of this type of image quality analysis need to be considered. When comparing the absolute CNR values of both studies using the 850.500 and 850.100 phantom, it stood out, that especially the values for the rod size of 0.75 mm considerably exceeded the values for the 0.8- and 0.9-millimeter rods of the 850.500 phantom. It can be assumed that this is mainly caused by the different number of rods. For future experiments, this should be compensated by providing the same number of capillaries for each diameter of the corresponding phantom.

Looking at the image quality, the comparison between the U-SPECT[5]/CT E-Class and U-SPECT[+]/CT revealed that the third lower detector could not show any advantages in this respect. Likewise, the systems are on par in terms of activity-dependent spatial resolution. However, the visual assessment of the image quality indicates a certain advantage of the new scanner, most likely to some degree due to the new reconstruction algorithm applied. On the other hand, this result is also supported by slightly higher absolute CNR values obtained with the two-headed system, although the deviation on average is only 3.6%. The evaluation of these two systems showed that the lack of a third detector is not a limitation for preclinical use. In conclusion, this method has proven that it could be a powerful tool for future image quality analyses, as it is easily transferable to other systems, making it easier to perform comparative analyses. With hot-rod phantoms being well-established for performance evaluations, this method is widely accessible without the need to purchase special-purpose phantoms.

Compared to the predecessor models U-SPECT-II and U-SPECT[+], the investigated U-SPECT[5] E-Class shows only minor deficits in terms of homogeneity and sensitivity [5,

49]. It is worth emphasizing, with respect to the competition, however, that the novel SPECT with its system design using stationary large-area detectors and multi-pinhole collimation achieves superior spatial resolution, especially in combination with sufficiently high sensitivity [93, 101, 104, 120]. For in vivo studies, it should be assumed that the reduced sensitivity can be compensated by increasing the administered tracer dose or scan time by 50%, but because the injection dose and volume or duration of anesthesia are strictly regulated by local animal welfare regulations and the animal's physiology, realization might be challenging [121]. Since the scan volume is defined based on images in three dimensions acquired either with a webcam or with X-rays, high resolutions can be achieved in studies for organ-specific targeted SPECT imaging as demonstrated by Branderhorst et al. [95, 122]. It is important to note that an improved resolution goes along with a loss of information outside of the selected scan volume. With this study, it could be shown that this system is very well-suited for preclinical imaging. The results are largely consistent with data from literature and confirm the advantages of multi-pinhole SPECT, as the trade-off between resolution and sensitivity is kept low and high detection efficiency can be upheld [123, 124]. For future projects, a similar performance evaluation of the U-SPECT[5] with an additional third detector would still be interesting to truly evaluate the potential benefits provided by the increased detection area. Since the experiments performed are limited to the main radioisotope ^{99m}Tc, it is proposed to complement the evaluation in the future with other isotopes such as ^{123}I, and ^{201}Tl and especially to further explore the possibilities of multi-isotope imaging studies as done for other systems [92]. When looking at stress/rest myocardial perfusion SPECT, especially the combination of ^{99m}Tc-sestamibi (stress) and [201]Tl (rest) is promising and already part of clinical practice [125]. First in vivo demonstrations with rats could already be performed, their extension to mouse studies might be of particular interest [126].

In this study, the capabilities of a dedicated small-animal SPECT system were assessed, equipped with two stationary detectors and interchangeable multi-pinhole collimators. Taking all the obtained results into consideration, it was possible to show, that the combination of the system design and improved image reconstruction despite lacking the third bottom detector does lead to excellent and competitive performance. With submillimeter spatial resolution paired with adequately high sensitivity, this system provides outstanding image quality and is a potent preclinical imaging tool for small rodents.

6. Summary

SPECT as a representative of molecular imaging allows visualization of metabolic processes in vivo. In clinical practice, single photon emission imaging is an established modality for myocardial perfusion imaging or the diagnosis of adrenal or neuroendocrine tumors, to name a few. With technical advances in scanner design and data processing leading to improved spatial resolution and image quality, SPECT has become a serious contender in small animal preclinical imaging. With multi-pinhole collimation, submillimeter spatial resolutions are achieved without limiting sensitivity, which has led to a significant increase of interest in SPECT for preclinical research in recent years.

In this dissertation, the potential of a two-detector system through an analysis of three dedicated mouse collimators with multi-pinhole configurations was demonstrated. For this, sensitivity, spatial resolution, and uniformity as key parameters were determined. In the second part of the present work, an evaluation of the image quality at different activity concentrations to allow prediction of the system performance related to in vivo studies was performed. Therefore, a visual evaluation, as well as a calculation of the contrast-to-noise ratio, was performed using mini Derenzo phantoms for the respective three mouse collimators. To better classify the results, the study was extended by a comparison with the predecessor system.

Due to the absence of the third bottom detector, sensitivity and uniformity are slightly compromised. All three collimators were able to achieve a spatial resolution in the submillimeter range, XUHR-M offers a peak resolution of up to 0.35 mm. In terms of resolution, both evaluated systems performed on an equal level. Visual assessment of image quality indicates a slight advantage of the new two-detector system, and the contrast-to-noise ratio seems to benefit from the improved SROSEM algorithm. However, the differences between the two systems are marginal.

The U-SPECT5/CT E-Class is proven to be state-of-the-art for small animal imaging and is a powerful instrument for preclinical molecular imaging research. Improvements in system design compensate well for the reduction in the detection area, allowing excellent imaging even with low activity concentrations.

SPECT als Vertreter der molekularen Bildgebung ermöglicht die Visualisierung von Stoffwechselprozessen in vivo. In der klinischen Praxis ist die Einzelphotonen-Emissions-Bildgebung eine etablierte Modalität für die Myokard-Perfusions-Bildgebung oder die Diagnose von Nebennieren- oder neuroendokrinen Tumoren, um nur einige Beispiele zu nennen. Mit den technischen Fortschritten bei der Konstruktion von Scannern und der Datenverarbeitung, die zu einer verbesserten räumlichen Auflösung und Bildqualität führen, ist SPECT zu einem ernstzunehmenden Mitbewerber in der präklinischen Bildgebung von Kleintieren geworden. Unter der Verwendung von Multipinhole-Kollimatoren lassen sich Ortsauflösungen von unter einem Millimeter erzielen, ohne die Sensitivität deutlich einzuschränken. Dies trug dazu bei, dass das Interesse an SPECT in der präklinischen Forschung in den letzten Jahren zugenommen hat.

In dieser Dissertation wurde das Potenzial eines Zweidetektorsystems unter Verwendung von drei Multipinhole-Mauskollimatoren evaluiert. Zur Leistungsbewertung wurde Sensitivität, Ortsauflösung und Homogenität bestimmt. Im zweiten Teil dieser Arbeit wurde eine Analyse der Bildqualität mit verschiedenen Aktivitätskonzentrationen durchgeführt, um eine Vorhersage der Leistung des Systems in In-vivo-Studien zu ermöglichen. Dazu wurde eine visuelle Bewertung sowie eine Berechnung des Kontrast-zu-Rausch-Verhältnisses mit Mini-Derenzo-Phantomen für die entsprechenden drei Mauskollimatoren durchgeführt. Um die Ergebnisse besser einordnen zu können, wurde die Studie um einen Vergleich mit dem Vorgängersystem erweitert.

Durch das Fehlen des dritten unteren Detektors sind Sensitivität und Homogenität leicht beeinträchtigt. Alle drei Kollimatoren konnten eine Ortsauflösung unter einem Millimeter erreichen, wobei XUHR-M die höchste Auflösung von bis zu 0.35 mm erreicht. Die beiden untersuchten Systeme sind hinsichtlich der Ortsauflösung gleichwertig. Die visuelle Bewertung der Bildqualität deutet auf einen leichten, jedoch nur marginalen Vorteil des neuen Zweidetektorsystems hin, und das Kontrast-zu-Rausch-Verhältnis scheint von dem verbesserten SROSEM-Algorithmus zu profitieren.

Das U-SPECT[5]/CT E-Class ist nachweislich auf dem neuesten Stand der Technik für die Bildgebung bei Kleintieren und ein leistungsfähiges Instrument für die präklinische Forschung. Das System kompensiert die Reduktion der Detektionsfläche und ermöglicht eine hervorragende Bildgebung auch bei geringen Aktivitätskonzentrationen.

7. References

[1]   G. Mariani and H. W. Strauss, "Positron emission and single-photon emission imaging: synergy rather than competition," (in eng), *Eur J Nucl Med Mol Imaging,* vol. 38, no. 7, pp. 1189-90, Jul 2011, doi: 10.1007/s00259-011-1767-3.

[2]   A. Rahmim and H. Zaidi, "PET versus SPECT: strengths, limitations and challenges," (in eng), *Nucl Med Commun,* vol. 29, no. 3, pp. 193-207, Mar 2008, doi: 10.1097/MNM.0b013e3282f3a515.

[3]   P. J. Slomka, T. Pan, D. S. Berman, and G. Germano, "Advances in SPECT and PET Hardware," *Prog Cardiovasc Dis,* vol. 57, no. 6, pp. 566-78, May-Jun 2015, doi: 10.1016/j.pcad.2015.02.002.

[4]   K. Van Audenhaege, R. Van Holen, and S. Vandenberghe, "Analysis of the trade-off between sensitivity and resolution of a pinhole collimator for SPECT," *Journal of Nuclear Medicine,* vol. 53, no. supplement 1, pp. 2410-2410, 2012.

[5]   O. Ivashchenko *et al.*, "Quarter-millimeter-resolution molecular mouse imaging with U-SPECT$^+$," (in eng), *Mol Imaging,* vol. 13, 2014, doi: 10.2310/7290.2014.00053.

[6]   M. C. Goorden *et al.*, "VECTor: a preclinical imaging system for simultaneous submillimeter SPECT and PET," *J Nucl Med,* vol. 54, no. 2, pp. 306-12, Feb 2013, doi: 10.2967/jnumed.112.109538.

[7]   Y. Lai *et al.*, "H(2)RSPET: a 0.5 mm resolution high-sensitivity small-animal PET scanner, a simulation study," *Phys Med Biol,* vol. 66, no. 6, p. 065016, Mar 9 2021, doi: 10.1088/1361-6560/abe558.

[8]   M. Melis, R. Valkema, E. P. Krenning, and M. de Jong, "Reduction of renal uptake of radiolabeled octreotate by amifostine coadministration," *J Nucl Med,* vol. 53, no. 5, pp. 749-53, May 2012, doi: 10.2967/jnumed.111.098665.

[9]   K. H. Ma *et al.*, "Dual SPECT of dopamine system using [99mTc]TRODAT-1 and [123I]IBZM in normal and 6-OHDA-lesioned formosan rock monkeys," (in eng), *Nucl Med Biol,* vol. 29, no. 5, pp. 561-7, Jul 2002, doi: 10.1016/s0969-8051(02)00303-7.

[10]   A. Nakazawa *et al.*, "Usefulness of dual 67Ga and 99mTc-sestamibi single-photon-emission CT scanning in the diagnosis of cardiac sarcoidosis," *Chest,* vol. 126, no. 4, pp. 1372-6, Oct 2004, doi: 10.1378/chest.126.4.1372.

[11]   A. Sanchez-Crespo *et al.*, "A novel quantitative dual-isotope method for simultaneous ventilation and perfusion lung SPET," *Eur J Nucl Med Mol Imaging,* vol. 29, no. 7, pp. 863-75, Jul 2002, doi: 10.1007/s00259-002-0803-8.

[12]   International Atomic Energy Agency, *Clinical Applications of SPECT/CT: New Hybrid Nuclear Medicine Imaging System.* Vienna: IAEA, 2008.

[13]   A. F. Chatziioannou, "Instrumentation for molecular imaging in preclinical research: Micro-PET and Micro-SPECT," *Proc Am Thorac Soc,* vol. 2, no. 6, pp. 533-6, 510-11, 2005, doi: 10.1513/pats.200508-079DS.

[14]   A. C. O'Farrell, S. D. Shnyder, G. Marston, P. L. Coletta, and J. H. Gill, "Non-invasive molecular imaging for preclinical cancer therapeutic development," *Br J Pharmacol,* vol. 169, no. 4, pp. 719-35, Jun 2013, doi: 10.1111/bph.12155.

[15]   M. R. Bernsen, P. E. Vaissier, R. Van Holen, J. Booij, F. J. Beekman, and M. de Jong, "The role of preclinical SPECT in oncological and neurological research in combination with either CT or MRI," *Eur J Nucl Med Mol Imaging,* vol. 41 Suppl 1, pp. S36-49, May 2014, doi: 10.1007/s00259-013-2685-3.

[16]   B. L. Franc, P. D. Acton, C. Mari, and B. H. Hasegawa, "Small-animal SPECT and SPECT/CT: important tools for preclinical investigation," (in eng), *J Nucl Med,* vol. 49, no. 10, pp. 1651-63, Oct 2008, doi: 10.2967/jnumed.108.055442.

[17]   H. Zaidi and B. Hasegawa, "Determination of the attenuation map in emission tomography," *J Nucl Med,* vol. 44, no. 2, pp. 291-315, Feb 2003.

[18]   S. C. Blankespoor *et al.*, "Attenuation correction of SPECT using X-ray CT on an emission-transmission CT system: myocardial perfusion assessment," *IEEE Transactions on Nuclear Science,* vol. 43, no. 4, pp. 2263-2274, 1996, doi: 10.1109/23.531891.

[19]   M. A. King *et al.*, "CHAPTER 22 - Attenuation, Scatter, and Spatial Resolution Compensation in SPECT," in *Emission Tomography*, M. N. Wernick and J. N. Aarsvold Eds. San Diego: Academic Press, 2004, pp. 473-498.

[20]   T. C. Lee, A. M. Alessio, R. M. Miyaoka, and P. E. Kinahan, "Morphology supporting function: attenuation correction for SPECT/CT, PET/CT, and PET/MR imaging," *Q J Nucl Med Mol Imaging,* vol. 60, no. 1, pp. 25-39, Mar 2016.

[21]   T. Schepis *et al.*, "Use of coronary calcium score scans from stand-alone multislice computed tomography for attenuation correction of myocardial perfusion SPECT," *Eur J Nucl Med Mol Imaging,* vol. 34, no. 1, pp. 11-9, Jan 2007, doi: 10.1007/s00259-006-0173-8.

[22]   T. Barwick *et al.*, "Single photon emission computed tomography (SPECT)/computed tomography using Iodine-123 in patients with differentiated thyroid cancer: additional value over whole body planar imaging and SPECT," *Eur J Endocrinol,* vol. 162, no. 6, pp. 1131-9, Jun 2010, doi: 10.1530/EJE-09-1023.

[23]   A. J. Einstein *et al.*, "Agreement of visual estimation of coronary artery calcium from low-dose CT attenuation correction scans in hybrid PET/CT and SPECT/CT with standard Agatston score," *J Am Coll Cardiol,* vol. 56, no. 23, pp. 1914-21, Nov 30 2010, doi: 10.1016/j.jacc.2010.05.057.

[24]   J. D. van Dijk *et al.*, "Value of attenuation correction in stress-only myocardial perfusion imaging using CZT-SPECT," *J Nucl Cardiol,* vol. 24, no. 2, pp. 395-401, Apr 2017, doi: 10.1007/s12350-015-0374-2.

[25]   W. C. Lavely *et al.*, "Comparison of SPECT/CT, SPECT, and planar imaging with single- and dual-phase (99m)Tc-sestamibi parathyroid scintigraphy," *J Nucl Med,* vol. 48, no. 7, pp. 1084-9, Jul 2007, doi: 10.2967/jnumed.107.040428.

[26]   Y. Zhang, B. Li, H. Shi, H. Yu, Y. Gu, and Y. Xiu, "Added value of SPECT/spiral CT versus SPECT or CT alone in diagnosing solitary skeletal lesions," *Nuklearmedizin,* vol. 56, no. 4, pp. 139-145, Aug 14 2017, doi: 10.3413/Nukmed-0886-17-03.

[27]   T. Derlin *et al.*, "Intraindividual comparison of 123I-mIBG SPECT/MRI, 123I-mIBG SPECT/CT, and MRI for the detection of adrenal pheochromocytoma in patients with elevated urine or plasma catecholamines," *Clin Nucl Med,* vol. 38, no. 1, pp. e1-6, Jan 2013, doi: 10.1097/RLU.0b013e318263923d.

[28]   T. Van den Wyngaert, F. Elvas, S. De Schepper, J. A. Kennedy, and O. Israel, "SPECT/CT: Standing on the Shoulders of Giants, It Is Time to Reach for the Sky!," *J Nucl Med,* vol. 61, no. 9, pp. 1284-1291, Sep 2020, doi: 10.2967/jnumed.119.236943.

[29]   O. Israel *et al.*, "Two decades of SPECT/CT - the coming of age of a technology: An updated review of literature evidence," *Eur J Nucl Med Mol Imaging,* vol. 46, no. 10, pp. 1990-2012, Sep 2019, doi: 10.1007/s00259-019-04404-6.

[30]   G. Mariani *et al.*, "A review on the clinical uses of SPECT/CT," *Eur J Nucl Med Mol Imaging,* vol. 37, no. 10, pp. 1959-85, Oct 2010, doi: 10.1007/s00259-010-1390-8.

[31]   J. V. Hoffmann *et al.*, "Performance evaluation of fifth-generation ultra-high-resolution SPECT system with two stationary detectors and multi-pinhole imaging," (in eng), *EJNMMI Phys,* vol. 7, no. 1, pp. 1-15, Nov 2 2020, Art no. 64, doi: 10.1186/s40658-020-00335-6. EJNMMI Phys.

[32]   O. Chiewitz and G. Hevesy, "Radioactive Indicators in the Study of Phosphorus Metabolism in Rats," *Nature,* vol. 136, no. 3445, pp. 754-755, 1935/11/01 1935, doi: 10.1038/136754a0.

[33]   F. A. Mettler, Jr., W. Huda, T. T. Yoshizumi, and M. Mahesh, "Effective doses in radiology and diagnostic nuclear medicine: a catalog," *Radiology,* vol. 248, no. 1, pp. 254-63, Jul 2008, doi: 10.1148/radiol.2481071451.

[34]   M. N. Wernick and J. N. Aarsvold, Eds. *Emission tomography the fundamentals of PET and SPECT*. Amsterdam: Elsevier Academic Press, 2004.

[35]   T. E. Peterson and L. R. Furenlid, "SPECT detectors: the Anger Camera and beyond," *Phys Med Biol,* vol. 56, no. 17, pp. R145-82, Sep 7 2011, doi: 10.1088/0031-9155/56/17/R01.

[36]   C. Levin, "CHAPTER 4 - Basic Physics of Radionuclide Imaging," in *Emission Tomography*, M. N. Wernick and J. N. Aarsvold Eds. San Diego: Academic Press, 2004, pp. 53-88.

[37]   G. L. Zeng, J. R. Galt, M. N. Wernick, R. A. Mintzer, and J. N. Aarsvold, "CHAPTER 7 - Single-Photon Emission Computed Tomography," in *Emission Tomography*, M. N. Wernick and J. N. Aarsvold Eds. San Diego: Academic Press, 2004, pp. 127-152.

[38]   R. Hofstadter, "The Detection of Gamma-Rays with Thallium-Activated Sodium Iodide Crystals," *Physical Review,* vol. 75, no. 5, pp. 796-810, 03/01/ 1949, doi: 10.1103/PhysRev.75.796.

[39]   I. Broser and H. Kallmann, "Über den Elementarprozeß der Lichtanregung in Leuchtstoffen durch α-Teilchen, schnelle Elektronen und γ-Quanten II," *Zeitschrift für Naturforschung A,* vol. 2, no. 11-12, pp. 642-650, 1947, doi: doi:10.1515/zna-1947-11-1206.

[40]   G. Dorenbos, D. O. Boerma, T. M. Buck, and G. H. Wheatley, "Au overlayer structures on a Ni(110) surface," *Phys Rev B Condens Matter,* vol. 51, no. 7, pp. 4485-4496, Feb 15 1995, doi: 10.1103/physrevb.51.4485.

[41]   F. Wilkinson, "CHAPTER 13 - Scintillators," in *Emission Tomography*, M. N. Wernick and J. N. Aarsvold Eds. San Diego: Academic Press, 2004, pp. 229-254.

[42] B. J. Pichler and S. I. Ziegler, "CHAPTER 14 - Photodetectors," in *Emission Tomography*, M. N. Wernick and J. N. Aarsvold Eds. San Diego: Academic Press, 2004, pp. 255-267.

[43] S. C. Moore, K. Kouris, and I. Cullum, "Collimator design for single photon emission tomography," *Eur J Nucl Med,* vol. 19, no. 2, pp. 138-50, 1992, doi: 10.1007/BF00184130.

[44] K. Van Audenhaege, R. Van Holen, S. Vandenberghe, C. Vanhove, S. D. Metzler, and S. C. Moore, "Review of SPECT collimator selection, optimization, and fabrication for clinical and preclinical imaging," *Med Phys,* vol. 42, no. 8, pp. 4796-813, Aug 2015, doi: 10.1118/1.4927061.

[45] S. R. Meikle, P. L. Kench, and J. Lin, "Design Considerations of Small-Animal SPECT Cameras," in *Molecular Imaging of Small Animals: Instrumentation and Applications*, H. Zaidi Ed. New York, NY: Springer New York, 2014, pp. 135-162.

[46] D. L. Gunter, "CHAPTER 8 - Collimator Design for Nuclear Medicine," in *Emission Tomography*, M. N. Wernick and J. N. Aarsvold Eds. San Diego: Academic Press, 2004, pp. 153-168.

[47] H. O. Anger, "Scintillation Camera with Multichannel Collimators," *J Nucl Med,* vol. 5, pp. 515-31, Jul 1964.

[48] G. Muehllehner, "A diverging collimator for gamma-ray imaging cameras," *J Nucl Med,* vol. 10, no. 4, pp. 197-201, Apr 1969.

[49] F. van der Have *et al.*, "U-SPECT-II: An Ultra-High-Resolution Device for Molecular Small-Animal Imaging," (in eng), *J Nucl Med,* vol. 50, no. 4, pp. 599-605, Apr 2009, doi: 10.2967/jnumed.108.056606.

[50] L. R. Furenlid *et al.*, "FastSPECT II: A Second-Generation High-Resolution Dynamic SPECT Imager," *IEEE Trans Nucl Sci,* vol. 51, no. 3, pp. 631-635, Jun 2004, doi: 10.1109/TNS.2004.830975.

[51] B. W. Miller, L. R. Furenlid, S. K. Moore, H. B. Barber, V. V. Nagarkar, and H. H. Barrett, "System Integration of FastSPECT III, a Dedicated SPECT Rodent-Brain Imager Based on BazookaSPECT Detector Technology," *IEEE Nucl Sci Symp Conf Rec (1997),* vol. Oct. 24 2009-Nov. 1 2009, pp. 4004-4008, Nov 1 2009, doi: 10.1109/NSSMIC.2009.5401924.

[52] K. Lin, I.-T. Hsiao, C. Wietholt, Y. Chung, C. Chen, and T. Yen, "Performance evaluation of an animal SPECT using modified NEMA standards," *Journal of Nuclear Medicine,* vol. 49, no. supplement 1, pp. 402P-402P, 2008.

[53]   N. U. Schramm, G. Ebel, U. Engeland, T. Schurrat, M. Behe, and T. M. Behr, "High-resolution SPECT using multipinhole collimation," *IEEE Transactions on Nuclear Science,* vol. 50, no. 3, pp. 315-320, 2003, doi: 10.1109/TNS.2003.812437.

[54]   W. Chang, C. E. Ordonez, H. Liang, Y. Li, and J. Liu, "C-SPECT - a Clinical Cardiac SPECT/Tct Platform: Design Concepts and Performance Potential," *IEEE Trans Nucl Sci,* vol. 56, no. 5, pp. 2659-2671, Oct 6 2009, doi: 10.1109/TNS.2009.2028138.

[55]   J. Dey, "Improvement of Performance of Cardiac SPECT Camera Using Curved Detectors With Pinholes," *IEEE Trans Nucl Sci,* vol. 59, no. 2, pp. 334-347, Apr 2012, doi: 10.1109/tns.2011.2182660.

[56]   T. Funk, D. L. Kirch, J. E. Koss, E. Botvinick, and B. H. Hasegawa, "A novel approach to multipinhole SPECT for myocardial perfusion imaging," *J Nucl Med,* vol. 47, no. 4, pp. 595-602, Apr 2006.

[57]   M. C. Goorden, M. C. Rentmeester, and F. J. Beekman, "Theoretical analysis of full-ring multi-pinhole brain SPECT," *Phys Med Biol,* vol. 54, no. 21, pp. 6593-610, Nov 7 2009, doi: 10.1088/0031-9155/54/21/010.

[58]   K. Van Audenhaege, S. Vandenberghe, K. Deprez, B. Vandeghinste, and R. Van Holen, "Design and simulation of a full-ring multi-lofthole collimator for brain SPECT," *Phys Med Biol,* vol. 58, no. 18, pp. 6317-36, Sep 21 2013, doi: 10.1088/0031-9155/58/18/6317.

[59]   H. O. Anger, "Scintillation Camera," *Review of Scientific Instruments,* vol. 29, no. 1, pp. 27-33, 1958, doi: 10.1063/1.1715998.

[60]   D. E. Kuhl and R. Q. Edwards, "Image Separation Radioisotope Scanning," *Radiology,* vol. 80, no. 4, pp. 653-662, 1963, doi: 10.1148/80.4.653.

[61]   D. E. Kuhl, J. Hale, and W. L. Eaton, "Transmission Scanning: A Useful Adjunct to Conventional Emission Scanning for Accurately Keying Isotope Deposition to Radiographic Anatomy," *Radiology,* vol. 87, no. 2, pp. 278-284, 1966, doi: 10.1148/87.2.278.

[62]   J. S. Fleming, "A technique for using CT images in attenuation correction and quantification in SPECT," *Nucl Med Commun,* vol. 10, no. 2, pp. 83-97, Feb 1989, doi: 10.1097/00006231-198902000-00002.

[63]   C. R. Meyer *et al.*, "Demonstration of accuracy and clinical versatility of mutual information for automatic multimodality image fusion using affine and thin-plate

spline warped geometric deformations," (in eng), *Med Image Anal,* vol. 1, no. 3, pp. 195-206, Apr 1997, doi: 10.1016/s1361-8415(97)85010-4.

[64]   T. Beyer, L. S. Freudenberg, D. W. Townsend, and J. Czernin, "The future of hybrid imaging-part 1: hybrid imaging technologies and SPECT/CT," *Insights Imaging,* vol. 2, no. 2, pp. 161-9, Apr 2011, doi: 10.1007/s13244-010-0063-2.

[65]   G. Crisan, N. S. Moldovean-Cioroianu, D. G. Timaru, G. Andries, C. Cainap, and V. Chis, "Radiopharmaceuticals for PET and SPECT Imaging: A Literature Review over the Last Decade," *Int J Mol Sci,* vol. 23, no. 9, Apr 30 2022, doi: 10.3390/ijms23095023.

[66]   International Atomic Energy Agency, *Technetium-99m Radiopharmaceuticals: Status and Trends* (IAEA Radioisotopes and Radiopharmaceuticals Series No. 1). Vienna: IAEA, 2010.

[67]   Nuclear Energy Agency, *The Supply of Medical Radioisotopes: 2018 Medical Isotope Demand and Capacity Projection for the 2018-2023 period*. Paris, France: OECD: Nuclear Energy Agency, 2018.

[68]   C. H. Green, "Technetium-99m production issues in the United Kingdom," *J Med Phys,* vol. 37, no. 2, pp. 66-71, Apr 2012, doi: 10.4103/0971-6203.94740.

[69]   National Research Council (U.S.). Committee on Medical Isotope Production Without Highly Enriched Uranium., *Medical isotope production without highly enriched uranium*. Washington, D.C.: National Academies Press, 2009.

[70]   National Academies of Sciences Engineering and Medicine: Committee on State of Molybdenum-99 Production and Utilization and Progress Toward Eliminating Use of Highly Enriched Uranium, *Molybdenum-99 for medical imaging*, Washington, DC: National Academies Press, 2016.

[71]   L. Bouwens, R. Van de Walle, H. Gifford, M. King, I. Lemahieu, and R. A. Dierckx, "LMIRA: list-mode iterative reconstruction algorithm for SPECT," *IEEE Transactions on Nuclear Science,* vol. 48, no. 4, pp. 1364-1370, 2001, doi: 10.1109/23.958356.

[72]   P. E. Kinahan, M. Defrise, and R. Clackdoyle, "CHAPTER 20 - Analytic Image Reconstruction Methods," in *Emission Tomography*, M. N. Wernick and J. N. Aarsvold Eds. San Diego: Academic Press, 2004, pp. 421-442.

[73]   D. S. Lalush and M. N. Wernick, "CHAPTER 21 - Iterative Image Reconstruction," in *Emission Tomography*, M. N. Wernick and J. N. Aarsvold Eds. San Diego: Academic Press, 2004, pp. 443-472.

[74] A. M. Cormack, "Representation of a Function by Its Line Integrals, with Some Radiological Applications," *Journal of Applied Physics,* vol. 34, no. 9, pp. 2722-2727, 1963, doi: 10.1063/1.1729798.

[75] A. M. Cormack, "Representation of a Function by Its Line Integrals, with Some Radiological Applications. II," *Journal of Applied Physics,* vol. 35, no. 10, pp. 2908-2913, 1964, doi: 10.1063/1.1713127.

[76] K. Lange and R. Carson, "EM reconstruction algorithms for emission and transmission tomography," *J Comput Assist Tomogr,* vol. 8, no. 2, pp. 306-16, Apr 1984.

[77] P. P. Bruyant, "Analytic and iterative reconstruction algorithms in SPECT," *J Nucl Med,* vol. 43, no. 10, pp. 1343-58, Oct 2002.

[78] H. E. Cline, W. E. Lorensen, S. Ludke, C. R. Crawford, and B. C. Teeter, "Two algorithms for the three-dimensional reconstruction of tomograms," *Medical Physics,* vol. 15, no. 3, pp. 320-327, 1988, doi: 10.1118/1.596225.

[79] H. M. Hudson and R. S. Larkin, "Accelerated image reconstruction using ordered subsets of projection data," *IEEE Transactions on Medical Imaging,* vol. 13, no. 4, pp. 601-609, 1994, doi: 10.1109/42.363108.

[80] W. Branderhorst, B. Vastenhouw, and F. J. Beekman, "Pixel-based subsets for rapid multi-pinhole SPECT reconstruction," (in eng), *Phys Med Biol,* vol. 55, no. 7, pp. 2023-34, Apr 2010, doi: 10.1088/0031-9155/55/7/015.

[81] P. E. Vaissier, F. J. Beekman, and M. C. Goorden, "Similarity-regulation of OS-EM for accelerated SPECT reconstruction," (in eng), *Phys Med Biol,* vol. 61, no. 11, pp. 4300-15, 06 2016, doi: 10.1088/0031-9155/61/11/4300.

[82] C.-M. Kao, P. L. RiviÈRe, and X. Pan, "CHAPTER 6 - Basics of Imaging Theory and Statistics," in *Emission Tomography*, M. N. Wernick and J. N. Aarsvold Eds. San Diego: Academic Press, 2004, pp. 103-126.

[83] M. N. Salihin Yusoff and A. Zakaria, "Determination of the optimum filter for qualitative and quantitative 99mTc myocardial SPECT imaging," (in eng), *International Journal of Radiation Research,* Original Research vol. 6, no. 4, pp. 173-182, 2009.

[84] M. Lyra and A. Ploussi, "Filtering in SPECT Image Reconstruction," (in eng), *Int J Biomed Imaging,* vol. 2011, p. 693795, 2011, doi: 10.1155/2011/693795.

[85] A. Signore, F. Jamar, O. Israel, J. Buscombe, J. Martin-Comin, and E. Lazzeri, "Clinical indications, image acquisition and data interpretation for white blood cells and anti-granulocyte monoclonal antibody scintigraphy: an EANM

procedural guideline," *Eur J Nucl Med Mol Imaging,* vol. 45, no. 10, pp. 1816-1831, Sep 2018, doi: 10.1007/s00259-018-4052-x.

[86]   T. Funk, P. Despres, W. C. Barber, K. S. Shah, and B. H. Hasegawa, "A multipinhole small animal SPECT system with submillimeter spatial resolution," *Med Phys,* vol. 33, no. 5, pp. 1259-68, May 2006, doi: 10.1118/1.2190332.

[87]   F. J. Beekman *et al.*, "U-SPECT-I: a novel system for submillimeter-resolution tomography with radiolabeled molecules in mice," *J Nucl Med,* vol. 46, no. 7, pp. 1194-200, Jul 2005.

[88]   B. Vastenhouw and F. Beekman, "Submillimeter total-body murine imaging with U-SPECT-I," (in eng), *J Nucl Med,* vol. 48, no. 3, pp. 487-93, Mar 2007.

[89]   O. Ivashchenko, F. van der Have, M. C. Goorden, R. M. Ramakers, and F. J. Beekman, "Ultra-high-sensitivity submillimeter mouse SPECT," (in eng), *J Nucl Med,* vol. 56, no. 3, pp. 470-5, Mar 2015, doi: 10.2967/jnumed.114.147140.

[90]   S. R. Meikle, P. Kench, M. Kassiou, and R. B. Banati, "Small animal SPECT and its place in the matrix of molecular imaging technologies," *Phys Med Biol,* vol. 50, no. 22, pp. R45-61, Nov 21 2005, doi: 10.1088/0031-9155/50/22/R01.

[91]   T. Niimi, M. Nanasato, M. Sugimoto, and H. Maeda, "Evaluation of Cadmium-Zinc-Telluride Detector-based Single-Photon Emission Computed Tomography for Nuclear Cardiology: a Comparison with Conventional Anger Single-Photon Emission Computed Tomography," *Nucl Med Mol Imaging,* vol. 51, no. 4, pp. 331-337, Dec 2017, doi: 10.1007/s13139-017-0474-9.

[92]   M. Lukas, A. Kluge, N. Beindorff, and W. Brenner, "Multi-Isotope Capabilities of a Small-Animal Multi-Pinhole SPECT System," *J Nucl Med,* vol. 61, no. 1, pp. 152-161, Jan 2020, doi: 10.2967/jnumed.119.226027.

[93]   S. Deleye, R. Van Holen, J. Verhaeghe, S. Vandenberghe, S. Stroobants, and S. Staelens, "Performance evaluation of small-animal multipinhole muSPECT scanners for mouse imaging," *Eur J Nucl Med Mol Imaging,* vol. 40, no. 5, pp. 744-58, May 2013, doi: 10.1007/s00259-012-2326-2.

[94]   N. Schramm, J. Hoppin, C. Lackas, F. Forrer, R. Valkema, and M. de Jong, "The NanoSPECT: A high-sensitivity multi-pinhole SPECT system with submillimeter (nanoliter) spatial resolution for imaging small rodents," *Journal of Nuclear Medicine,* vol. 47, no. suppl 1, pp. 233P-233P, 2006.

[95]   W. Branderhorst, B. Vastenhouw, F. van der Have, E. L. Blezer, W. K. Bleeker, and F. J. Beekman, "Targeted multi-pinhole SPECT," (in eng), *Eur J Nucl Med*

Mol Imaging, vol. 38, no. 3, pp. 552-61, Mar 2011, doi: 10.1007/s00259-010-1637-4.

[96] National Electrical Manufacturers Association, *NEMA Standards Publication NU 1-2018: Performance Measurements of Gamma Cameras*. National Electrical Manufacturers Association, 2018.

[97] National Electrical Manufacturers Association, *NEMA Standards Publication NU 4-2008: Performance Measurements of Small Animal Positron Emission Tomographs*. National Electrical Manufacturers Association, 2008.

[98] MILabs B.V., "User Manual: U-SPECT5 U-SPECT5CT U-PET5 U-PET5CT U-CT VECTor5 VECTor5CT," Utrecht, The Netherlands, 2018.

[99] F. van der Have, B. Vastenhouw, M. Rentmeester, and F. J. Beekman, "System calibration and statistical image reconstruction for ultra-high resolution stationary pinhole SPECT," (in eng), *IEEE Trans Med Imaging,* vol. 27, no. 7, pp. 960-71, 2008, doi: 10.1109/tmi.2008.924644. IEEE Trans Med Imaging.

[100] P. E. Vaissier, M. C. Goorden, B. Vastenhouw, F. van der Have, R. M. Ramakers, and F. J. Beekman, "Fast spiral SPECT with stationary gamma-cameras and focusing pinholes," *J Nucl Med,* vol. 53, no. 8, pp. 1292-9, Aug 2012, doi: 10.2967/jnumed.111.101899.

[101] F. Boisson *et al.*, "Imaging capabilities of the Inveon SPECT system using single-and multipinhole collimators," *J Nucl Med,* vol. 54, no. 10, pp. 1833-40, Oct 2013, doi: 10.2967/jnumed.112.117572.

[102] K. Magota, N. Kubo, Y. Kuge, K. Nishijima, S. Zhao, and N. Tamaki, "Performance characterization of the Inveon preclinical small-animal PET/SPECT/CT system for multimodality imaging," *Eur J Nucl Med Mol Imaging,* vol. 38, no. 4, pp. 742-52, Apr 2011, doi: 10.1007/s00259-010-1683-y.

[103] R. J. Jaszczak, J. Li, H. Wang, M. R. Zalutsky, and R. E. Coleman, "Pinhole collimation for ultra-high-resolution, small-field-of-view SPECT," *Phys Med Biol,* vol. 39, no. 3, pp. 425-37, Mar 1994, doi: 10.1088/0031-9155/39/3/010.

[104] I. Matsunari *et al.*, "Performance evaluation of the eXplore speCZT preclinical imaging system," *Ann Nucl Med,* vol. 28, no. 5, pp. 484-97, Jun 2014, doi: 10.1007/s12149-014-0828-7.

[105] M. P. Unterweger and R. Fitzgerald, "Corrigendum to "Update of NIST half-life results corrected for ionization chamber source-holder instability" [Appl. Radiat. Isot. 87 (2014) 92-94]," *Appl Radiat Isot,* vol. 159, p. 108976, May 2020, doi: 10.1016/j.apradiso.2019.108976.

[106] H. Krieger, *Grundlagen der Strahlungsphysik und des Strahlenschutzes*, 6 ed. Berlin, Heidelberg: Springer Spektrum, 2019.

[107] H. Wieczorek, "SPECT Image Quality and Quantification," in *2006 IEEE Nuclear Science Symposium Conference Record*, 29 Oct.-1 Nov. 2006 2006, vol. 5, pp. 2854-2858, doi: 10.1109/NSSMIC.2006.356472.

[108] L. A. Shepp and Y. Vardi, "Maximum likelihood reconstruction for emission tomography," (in eng), *IEEE Trans Med Imaging,* vol. 1, no. 2, pp. 113-22, 1982, doi: 10.1109/TMI.1982.4307558.

[109] K. Ogawa, Y. Harata, T. Ichihara, A. Kubo, and S. Hashimoto, "A practical method for position-dependent Compton-scatter correction in single photon emission CT," *IEEE Trans Med Imaging,* vol. 10, no. 3, pp. 408-12, 1991, doi: 10.1109/42.97591.

[110] S. C. Kappadath, "Effects of voxel size and iterative reconstruction parameters on the spatial resolution of 99mTc SPECT/CT," *J Appl Clin Med Phys,* vol. 12, no. 4, p. 3459, Nov 15 2011, doi: 10.1120/jacmp.v12i4.3459.

[111] M. D. Walker *et al.*, "Performance assessment of a preclinical PET scanner with pinhole collimation by comparison to a coincidence-based small-animal PET scanner," (in eng), *J Nucl Med,* vol. 55, no. 8, pp. 1368-74, Aug 2014, doi: 10.2967/jnumed.113.136663.

[112] A. M. Loening and S. S. Gambhir, "AMIDE: a free software tool for multimodality medical image analysis," (in eng), *Mol Imaging,* vol. 2, no. 3, pp. 131-7, Jul 2003.

[113] P. Vaissier, M. Goorden, and F. Beekman, "Similarity-Regulated OSEM reconstruction for pinhole-PET," *Journal of Nuclear Medicine,* vol. 56, no. supplement 3, pp. 48-48, 2015.

[114] A. A. Attarwala *et al.*, "Performance assessment of the ALBIRA II pre-clinical SPECT S102 system for (99m)Tc imaging," *Ann Nucl Med,* vol. 35, no. 1, pp. 111-120, Jan 2021, doi: 10.1007/s12149-020-01547-7.

[115] G. S. Mitchell and S. R. Cherry, "A high-sensitivity small animal SPECT system," *Phys Med Biol,* vol. 54, no. 5, pp. 1291-305, Mar 7 2009, doi: 10.1088/0031-9155/54/5/013.

[116] B. A. Harkness, W. L. Rogers, N. H. Clinthorne, and J. W. Keyes, Jr., "SPECT: Quality Control Procedures and Artifact Identification," *J Nucl Med Technol,* vol. 11, pp. 55-60, 1983.

[117]   M. P. Nguyen, M. C. Goorden, C. Kamphuis, and F. J. Beekman, "Evaluation of pinhole collimator materials for micron-resolution ex vivo SPECT," *Phys Med Biol,* vol. 64, no. 10, p. 105017, May 16 2019, doi: 10.1088/1361-6560/ab1618.

[118]   G. S. P. Mok, J. Yu, Y. Du, Y. Wang, and B. M. W. Tsui, "Evaluation of a Multi-pinhole Collimator for Imaging Small Animals with Different Sizes," *Molecular Imaging and Biology,* vol. 14, no. 1, pp. 60-69, 2012/02/01 2012, doi: 10.1007/s11307-011-0472-8.

[119]   G. S. Mok, Y. Wang, and B. M. Tsui, "Quantification of the Multiplexing Effects in Multi-Pinhole Small Animal SPECT: A Simulation Study," *IEEE Trans Nucl Sci,* vol. 56, no. 5, pp. 2636-2643, 2009, doi: 10.1109/TNS.2009.2023444.

[120]   V. Moji *et al.*, "Performance evaluation of a newly developed high-resolution, dual-head animal SPECT system based on the NEMA NU1-2007 standard," *J Appl Clin Med Phys,* vol. 15, no. 6, p. 4936, Nov 8 2014, doi: 10.1120/jacmp.v15i6.4936.

[121]   K. H. Diehl *et al.*, "A good practice guide to the administration of substances and removal of blood, including routes and volumes," *J Appl Toxicol,* vol. 21, no. 1, pp. 15-23, Jan-Feb 2001, doi: 10.1002/jat.727.

[122]   W. Branderhorst, F. van der Have, B. Vastenhouw, M. A. Viergever, and F. J. Beekman, "Murine cardiac images obtained with focusing pinhole SPECT are barely influenced by extra-cardiac activity," *Phys Med Biol,* vol. 57, no. 3, pp. 717-32, Feb 7 2012, doi: 10.1088/0031-9155/57/3/717.

[123]   F. Beekman and F. van der Have, "The pinhole: gateway to ultra-high-resolution three-dimensional radionuclide imaging," (in eng), *Eur J Nucl Med Mol Imaging,* vol. 34, no. 2, pp. 151-61, Feb 2007, doi: 10.1007/s00259-006-0248-6.

[124]   J. P. Islamian, A. Azazrm, B. Mahmoudian, and E. Gharapapagh, "Advances in pinhole and multi-pinhole collimators for single photon emission computed tomography imaging," *World J Nucl Med,* vol. 14, no. 1, pp. 3-9, Jan-Apr 2015, doi: 10.4103/1450-1147.150505.

[125]   T. Sharir and P. Slomka, "Dual-isotope myocardial perfusion SPECT imaging: Past, present, and future," *Journal of Nuclear Cardiology,* vol. 25, no. 6, pp. 2024-2028, 2018/12/01 2018, doi: 10.1007/s12350-017-0966-0.

[126]   J. P. Janssen *et al.*, "Capabilities of multi-pinhole SPECT with two stationary detectors for in vivo rat imaging," (in eng), *Sci Rep,* vol. 10, no. 1, p. 18616, Oct 29 2020, doi: 10.1038/s41598-020-75696-0. Sci Rep.

Appendix

I. Abbreviations

2D .... two-dimensional

3D .... three-dimensional

BP .... bed position

CFOV .... central field of view

CHFC .... Comprehensive Heart Failure Center

CNR .... contrast-to-noise ratio

cps .... counts per second

CT .... computed tomography

CZT .... cadmium zinc telluride

FBP .... filtered back projection

FOV .... field of view

FWHM .... full width at half maximum

GP-M .... general purpose mouse imaging

it .... iteration

LOR .... line of response

MLEM .... maximum-likelihood expectation-maximization

MRI .... magnetic resonance imaging

NaI(Tl) .... thallium-doped sodium iodide

NEMA .... National Electrical Manufacturers Association

NoU .... number of updates

OSEM .... ordered subset expectation maximization

PET .... positron emission tomography

PMT .... photomultiplier tube

POSEM .... pixel-based ordered subset expectation maximization

ROI .... region of interest

sb .... subset

SFM .... scanning focus method

SPECT .... single photon emission computed tomography

SROSEM .... similarity-regulated ordered subset expectation maximization

$t_{1/2}$ .... half-life

TEW .... triple energy window

TPB .... time per bed position

II. List of Figures

III. List of Tables

IV.Acknowledgment

V. Personal Publications and Congress Attendances

Personal Publications:

(1) J. V. Hoffmann *et al.*, "Performance evaluation of fifth-generation ultra-high-resolution SPECT system with two stationary detectors and multi-pinhole imaging," (in eng), *EJNMMI Phys,* vol. 7, no. 1, p. 64, Nov 2 2020, doi: 10.1186/s40658-020-00335-6. EJNMMI Phys.

(2) J. P. Janssen *et al.*, "Capabilities of multi-pinhole SPECT with two stationary detectors for in vivo rat imaging," (in eng), *Sci Rep,* vol. 10, no. 1, p. 18616, Oct 29 2020, doi: 10.1038/s41598-020-75696-0. Sci Rep.

Congress Attendances:

(1) J. V. Hoffmann, J. P. Janssen, T. Kanno, and T. Higuchi, "Performance evaluation of U-SPECT5 E-Class: multi-pinhole imaging with 2 stationary detectors," presented at the *European Molecular Imaging Meeting - EMIM 2020*, Virtual Edition, August 24th - 25th, 2020, Poster, 803.

(2) J. V. Hoffmann, J. P. Janssen, T. Kanno, and T. Higuchi, "Performance of a Novel Small-Animal SPECT System with Two Stationary Detectors: A Comparison of Multi-Pinhole Collimators for Mouse Imaging," presented at the *33rd Annual Congress of the European Association of Nuclear Medicine - EANM'20*, Virtual Edition, October 22nd - 30th, 2020, Oral Presentation, OP-908.

VI.Curriculum Vitae